

AD-A016 929

INCREASED ROTOR BLADE SURVIVABILITY

C. F. Griffin

Lockheed-California Company

Prepared for:

Army Air Mobility Research and Development Laboratory

August 1975

DISTRIBUTED BY:

NTIS

National Technical Information Service
U. S. DEPARTMENT OF COMMERCE

317120

USAAMRDL-TR-75-6

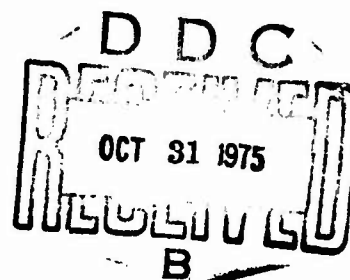


INCREASED ROTOR BLADE SURVIVABILITY

AD A 016929

Lockheed-California Company
Burbank, Calif. 91520

August 1975



Final Report for Period 1 July 1973 - 1 July 1975

Approved for public release;
distribution unlimited.

Prepared for

EUSTIS DIRECTORATE

U. S. ARMY AIR MOBILITY RESEARCH AND DEVELOPMENT LABORATORY


Fort Eustis, Va. 23604

Reproduced by
NATIONAL TECHNICAL
INFORMATION SERVICE
US Department of Commerce
Springfield, VA. 22151

EUSTIS DIRECTORATE POSITION STATEMENT

This report is considered to provide a survivable design approach of a composite helicopter main rotor blade that appears promising as being ballistic-damage-tolerant of 23mm HEI-T type projectile impacts. The blade concept of a geodesic-celled elliptical beam spar greater than half the chord length, made of graphite yarn in a grid network pattern featuring multiload paths, high strength, and light weight, plus a frangible aerodynamic fiberglass skin, tends to alleviate the explosive damaging effects of the projectile. Results of this contractual effort are still preliminary, and additional effort is required to improve and validate the survivable characteristics of the design. The data will aid in advancing the state of the art of helicopter survivability against light antiaircraft threats.

Mr. Stephen Pociluyko of the Military Operation Technology Division served as the technical monitor for this effort.

ACCESSION for	
NTIS	White & Olson <input checked="" type="checkbox"/>
DDC	D. C. Olson <input type="checkbox"/>
UNCLASSIFIED	<input type="checkbox"/>
JUSTIFICATION	
BY	
DISSEMINATION AUTHORITY CDS	
Dist.	Avail. Prior Special
	

DISCLAIMERS

The findings in this report are not to be construed as an official Department of the Army position unless so designated by other authorized documents.

When Government drawings, specifications, or other data are used for any purpose other than in connection with a definitely related Government procurement operation, the United States Government thereby incurs no responsibility nor any obligation whatsoever; and the fact that the Government may have formulated, furnished, or in any way supplied the said drawings, specifications, or other data is not to be regarded by implication or otherwise as in any manner licensing the holder or any other person or corporation, or conveying any rights or permission, to manufacture, use, or sell any patented invention that may in any way be related thereto.

Trade names cited in this report do not constitute an official endorsement or approval of the use of such commercial hardware or software.

DISPOSITION INSTRUCTIONS

Destroy this report when no longer needed. Do not return it to the originator.

UNCLASSIFIED

SECURITY CLASSIFICATION OF THIS PAGE (When Data Entered)

REPORT DOCUMENTATION PAGE		READ INSTRUCTIONS BEFORE COMPLETING FORM
1. REPORT NUMBER USAAMRDL-TR-75-6	2. GOVT ACCESSION NO.	3. RECIPIENT'S CATALOG NUMBER
4. TITLE (and Subtitle) INCREASED ROTOR BLADE SURVIVABILITY		5. TYPE OF REPORT & PERIOD COVERED 7-1-73 to 7-1-75 Final
7. AUTHOR(s) C. F. GRIFFIN		6. PERFORMING ORG. REPORT NUMBER LR 26700
9. PERFORMING ORGANIZATION NAME AND ADDRESS Lockheed-California Company Burbank, California 91520		8. CONTRACT OR GRANT NUMBER(s) DAAJ02-73-C-0101
11. CONTROLLING OFFICE NAME AND ADDRESS EUSTIS DIRECTORATE U. S. Army Air Mobility R&D Laboratory Fort Eustis, Va. 23604		10. PROGRAM ELEMENT, PROJECT, TASK AREA & WORK UNIT NUMBERS 63208A 1F163208DB52 00 002 EK
14. MONITORING AGENCY NAME & ADDRESS (if different from Controlling Office)		12. REPORT DATE August 1975
		13. NUMBER OF PAGES 88
		15. SECURITY CLASS. (of this report) UNCLASSIFIED
		15a. DECLASSIFICATION/DOWNGRADING SCHEDULE
16. DISTRIBUTION STATEMENT (of this Report) Approved for public release; distribution unlimited.		
17. DISTRIBUTION STATEMENT (of the abstract entered in Block 20, if different from Report)		
19. SUPPLEMENTARY NOTES		
19. KEY WORDS (Continue on reverse side if necessary and identify by block number) Survivability, Composites, Geodesic Structure, Graphite/Epoxy		
20. ABSTRACT (Continue on reverse side if necessary and identify by block number) Reported are results of a program to investigate the feasibility of using composite geodesic structure for the blade spar to increase survivability of helicopter main rotor blades. The design investigated consists of a geodesic truss structure spar of elliptical cross section comprised of elements forming a redundant grid-work. This spar is covered with a thin composite expendable skin that		

DD FORM 1473 1 JAN 73 EDITION OF 1 NOV 65 IS OBSOLETE

UNCLASSIFIED

SECURITY CLASSIFICATION OF THIS PAGE (When Data Entered)

UNCLASSIFIED

SECURITY CLASSIFICATION OF THIS PAGE(When Data Entered)

forms the airfoil contour. Parametric analyses were conducted to determine the effects of geometry and materials on the strength and stiffness of geodesic structures. Subscale sections of the graphite/epoxy geodesic main rotor blade box spar were fabricated and tested. A graphite/epoxy geodesic helicopter main rotor blade preliminary design was completed, and four full-scale segments of this blade were fabricated and subjected to structural and ballistic tests.

ii
UNCLASSIFIED

SECURITY CLASSIFICATION OF THIS PAGE(When Data Entered)

SUMMARY

The primary ballistic threat for helicopter main rotor blades is 23mm High Explosive Incendiary Tracer (HEI-T) projectiles. Reported are results of a research and development program to investigate the feasibility of using composite geodesic structure for the blade spar to increase survivability of helicopter main rotor blades against this threat.

The design investigated consists of a graphite/epoxy geodesic truss structure spar of elliptical cross section. This spar is covered with a thin composite expendable skin that forms the airfoil contour. Parametric analyses were conducted to determine the effects of geometry and materials on the strength and stiffness of geodesic structures. Four subscale geodesic blade spars were fabricated and statically tested. Strength characteristics were lower than analytically predicted. It is believed that the hand-winding fabrication process contributed significantly to the discrepancies between actual structural behavior and predicted test results.

Test results and manufacturing experience obtained from the subscale box spar specimens were used for the conceptual design of a geodesic main rotor blade for the AH-56A Cheyenne compound helicopter. The basic design philosophy was to extend the geodesic spar over 50% of the blade chord and to use the frangibility of the skin to relieve the projectile blast pressure, thereby reducing damage effects. Four full-scale segments of this blade were fabricated. Three blade specimens were ballistically tested. These limited tests demonstrated the feasibility of using the geodesic open grid/frangible skin approach to minimize damage to the structure by small HE projectiles. An undamaged blade specimen and a ballistically damaged blade specimen were subjected to fatigue testing followed by residual strength testing. The damaged blade was fatigue tested for an equivalent of more than 23 flight hours without failure at blade loads characteristic of maximum level-flight velocity. The residual static strength of the damaged blade was 45% of the undamaged blade. These tests demonstrated the feasibility of the geodesic design concept to increase helicopter main rotor blade survivability.

PREFACE

This report was prepared by the Lockheed-California Company Rotary Wing Technology Department for the Eustis Directorate, U. S. Army Air Mobility Research and Development Laboratory, Fort Eustis, Virginia. Mr. Stephen Pociluyko was the U. S. Army program monitor.

The work reported was conducted by the Lockheed-California Company from July 1973 to June 1975 under Contract DAAJ02-73-C-0101. The principal investigator for the program was Mr. C. F. Griffin, and all manufacturing research activities were coordinated by Mr. L. Blad.

Guidance of the program was provided by Dr. E. R. Wood of the Lockheed-California Company and Mr. I. E. Figge of the Eustis Directorate. Appreciation is also due Mr. P. Kesling and Mr. C. Axtell of Lockheed for their helpful criticism during the project.

Preceding page blank

TABLE OF CONTENTS

	<u>Page</u>
SUMMARY	1
PREFACE	3
LIST OF ILLUSTRATIONS	6
LIST OF TABLES	9
INTRODUCTION	10
STRUCTURAL CHARACTERIZATION	12
Description and Design Considerations	12
Parametric Analysis	15
Damage Tolerance	23
SPECIMEN FABRICATION AND TESTS	31
Fabrication and Test Plan	31
Tooling and Fabrication	31
Test Results	33
ROTOR BLADE	41
Design	41
Specimen Design and Fabrication	42
Ballistic Tests	47
Structural Tests	56
CONCLUSIONS	67
RECOMMENDATIONS	68
REFERENCES	69
APPENDIX A. COMPUTER PROGRAM FOR GEODESIC PLATES	70
LIST OF SYMBOLS	82

Preceding page blank

LIST OF ILLUSTRATIONS

<u>Figure</u>		<u>Page</u>
1	Geodesic Structural Concept	13
2	Cross Section of a Typical Two-Element Intersection .	14
3	Schematic of $\pm\phi$, 90° Element Pattern	18
4	Axial Stiffness Parameter for Panels With Elements at $\pm\phi$, 90°	18
5	Axial Strength Parameter for Panels With Elements at $\pm\phi$, 90°	20
6	Shear Stiffness Parameter for Panels With Elements at $\pm\phi$, 90°	20
7	Schematic of 0° , $\pm 30^\circ$, 90° Element Pattern.	21
8	Axial Stiffness Parameter for Panels With Elements at 0° , $\pm 30^\circ$, 90°	21
9	Axial Strength Parameter for Panels With Elements at 0° , $\pm 30^\circ$, 90°	22
10	Shear Stiffness Parameter for Panels With Elements at 0° , $\pm 30^\circ$, 90°	22
11	Specific Axial Stiffness of $\pm 30^\circ$, 90° Panels.	24
12	Specific Axial Strength of $\pm 30^\circ$, 90° Panels	25
13	Specific Axial Stiffness of 0° , $\pm 30^\circ$, 90° Panels. . .	26
14	Schematic of a Geodesic Plate Containing Ballistic Damage	28
15	Residual Strength of a Geodesic Panel With 66.7% $\pm 30^\circ$ and 33.33% 90° Elements.	30
16	Tooling for Beam Specimens	32
17	Graphite/Epoxy Beam Specimen.	32
18	Load Strain Curve for a Single-Element Specimen . . .	35

LIST OF ILLUSTRATIONS (Continued)

<u>Figure</u>		<u>Page</u>
19	Three-Cell-Wide Plate Specimen	36
20	Failed Plate Specimen	36
21	Test Setup for Beam Specimen	38
22	Load-Strain Curves for Beam Specimen Elements	39
23	Conceptual Design of a Geodesic Rotor Blade	43
24	Geodesic Blade Segment Design	45
25	Graphite/Epoxy Blade Spar	48
26	Geodesic Rotor Blade Segment	48
27	Ballistic Range	49
28	Entry Damage - Specimen 1	50
29	Exit Damage - Specimen 1	50
30	Ballistic Damage to Specimen 1	51
31	Entry Damage - Specimen 2	51
32	Exit Damage - Specimen 2	53
33	Damage to Metal Blade Caused By Ballistic Impact Similar to That Used on Specimen 2	53
34	Ballistic Damage to Specimen 2	54
35	Entry Damage - Specimen 3	54
36	Exit Damage - Specimen 3	55
37	Ballistic Damage to Specimen 3	55
38	Undamaged Blade Installed in Fatigue Test Machine	58
39	Exit Side of Damaged Blade After 327,000 Cycles of Load	58

LIST OF ILLUSTRATIONS (Continued)

<u>Figure</u>		<u>Page</u>
40	Residual Strength Test Apparatus	61
41	Undamaged Blade Specimen Aluminum End Grip Plate Failure	61
42	Undamaged Blade Specimen After Residual Strength Test	62
43	Fractured Surface in Geodesic Spar in Undamaged Blade Specimen	62
44	Undamaged Blade - Load-Strain Response	63
45	Damaged Blade Specimen After Residual Strength Test .	63
46	Fractured Surface in Geodesic Spar, Exit Side	64
47	Damaged Blade - Load-Strain Response.	64
A-1	Program Listing	72
A-2	Isogrid Structure From Example 1	77
A-3	Computer Input, Example 1	78
A-4	Computer Output, Example 1	79
A-5	Computer Input, Example 2	80
A-6	Computer Output, Example 2.	81

LIST OF TABLES

<u>Table</u>		<u>Page</u>
1	Fiber Material Properties	19
2	Predicted Damage Tolerance of Geodesic Plates . . .	29
3	Single-Element Specimen Test Results	34
4	Plate Specimen Test Results	37
5	Beam Specimen Test Results.	37
6	Summary of Fatigue Tests on Undamaged Blade	59
7	Summary of Fatigue Tests on Damaged Blade	60
8	Summary of Residual Strength Tests	65

INTRODUCTION

The primary threat for helicopter main rotor blades is 23mm High Explosive Incendiary Tracer (HEI-T) projectiles. Test data gathered at military test facilities and independent tests conducted by the Lockheed-California Company indicate that conventional metallic rotor blades are not survivable against this threat. Thus, innovations in blade design are required to achieve a more damage-tolerant structure.

A more survivable rotor blade is offered by a truss structure spar design comprised of elements forming an elliptical-shaped beam with a redundant gridwork covered by an aerodynamic skin. In contrast to a conventional uniform isotropic blade spar, geodesic construction is used because of its crack-insensitive nature. This concept provides a multiplicity of load paths so that projectile fragments, while cutting structure over a large area, leave sufficient load paths to carry normal flight loads. The structurally expendable skin tears cut locally, allowing venting of the pressure wave initiated by the explosion of the projectile.

The structural efficiency and damage-tolerant characteristics inherent in geodesic and waffle-stiffened skin construction have long been recognized. For example, the geodesic design approach was used for survivability in military aircraft as early as 1936 in the Vickers Wellington Bomber, which had a wood airframe configured entirely of geodesic structure.¹ Research into the structural behavior of metallic waffle-stiffened skin construction is described in References 2, 3 and 4.

The major disadvantage experienced with this type of construction is the amount of assembly time or machining required to fabricate the structure using conventional materials. Recently, several organizations have taken advantage of the manufacturing flexibility offered by fibrous composite materials and investigated the use of these materials for the construction of geodesic structures. For example, a three-dimensional orientated space frame composite structure, Tetra-Core, was developed at the Eustis Directorate of the U. S. Army Air Mobility Research and Development Laboratory.² Several components have been fabricated with Tetra-Core. These include a ballistic-damage-tolerant helicopter bell crank lever. Ballistic impacts on the bell crank, followed by fatigue testing, demonstrated the fail-safe characteristics of the structural concept.⁶

The research described herein concerns fibrous composite geodesic structures and methods used to fabricate these structures. Because the structural configuration represents a radical departure from laminated composite structures, an analytic structural characterization of composite geodesic panels was conducted. To verify the structural

capability of a typical composite geodesic structure, specimens were fabricated and tested. Results of the analytical and experimental investigation into the structural behavior of damaged and undamaged composite geodesic structures were used to design a helicopter main rotor blade that would be damage-tolerant of the effects of a 23mm HEI-T projectile impact. Since the principal objective of the research was an experimental determination of the feasibility of using composite geodesic structures to increase the survivability of helicopter main rotor blades, four full-scale segments of the geodesic rotor blade were fabricated. Three segments were ballistically tested. Fatigue and residual strength tests were conducted on a ballistically damaged blade specimen and on an undamaged blade specimen.

STRUCTURAL CHARACTERIZATION

DESCRIPTION AND DESIGN CONSIDERATIONS

A main rotor blade design which offers increased survivability consists of a truss structure box spar comprised of many elements forming a redundant gridwork covered with an aerodynamic skin. The principal advantages of this structure derive from its crack-insensitive nature and the fact that the structurally expendable skin tears out locally, allowing venting of the pressure wave initiated by the explosion of the projectile.

The structural concept investigated in this study involves the use of a spatial truss structure consisting of continuous internal members which intersect to form a waffle-like pattern as shown in Figure 1. Internal members or elements of the structure are composed of uni-directional filamentary composite materials which are continuous through the intersections or nodes.

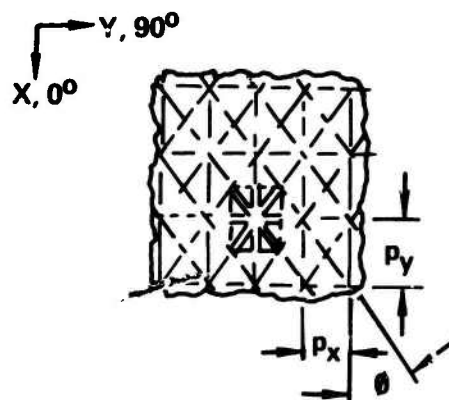
A rotor blade designed on the basis of this structural concept is an elliptical cross-section spar with surfaces composed of longitudinal, helical, and circumferential elements.

If the spar is subjected to a torsional load, all of the helical elements in one direction are in tension and the helical elements in the other direction are in compression. Forces normal to the surface of the tube are induced at the intersection of the elements, tending to maintain the original contour of the elements.

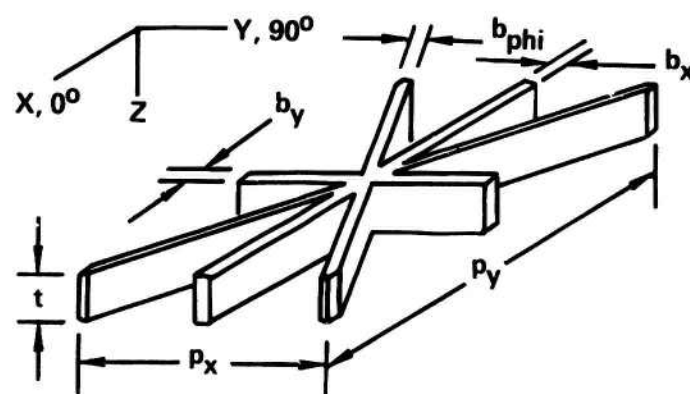
Longitudinal loading on the spar is reacted by the longitudinal members and the helical members. In this case the circumferential members supply lateral support to the helical members to inhibit their collapse, and provide a semicontinuous foundation for the intersection. Without the circumferential elements, only the longitudinal elements react the longitudinal loading.

Note that elements within the structure are subject to bending and axial forces. As spacing between elements decreases, conditions approach the ideal state of continuous support wherein the elements will be subject to axial forces only.

For the elliptical tube to react both torsional and longitudinal loads, it must have helical elements and either longitudinal or circumferential elements, or both. A structure with helical and circumferential elements or helical and longitudinal elements will contain two- and three-element intersections. With longitudinal, helical and circumferential elements present, the structure will have two-, three-, and four-element intersections. The number of elements which intersect at a node becomes important when one considers the construction of a typical element.



a) TYPICAL GRID PATTERN (SHORT DASHED LINES ENCLOSE TYPICAL CELL)



b) THREE-DIMENSIONAL VIEW OF TYPICAL CELL

Figure 1. Geodesic Structural Concept.

If the elements of the geodesic structure consist of fiber bundles separated by resin, and the elements and nodes have identical heights, then the fiber volume within each element is proportional to the number of elements which intersect at a node. For example, if the fiber bundle has 60% fiber volume, then the elements in a structure which contains two-element intersections will have 30% fiber volume; three-elements intersections, 20% fiber volume; and four-element intersections, 15% fiber volume. The modulus and strength of the element are proportional to the volume of fibers within the element. This emphasizes the importance of nodal geometry on structural efficiency of the geodesic elements.

Early experiments with various numbers of composite elements intersecting at a node (with winding and autoclave pressure) indicate that fiber bundles tend to flatten in the nodes, as shown in the two-element intersection in Figure 2. This results in fiber volumes within the elements approximately twice the magnitude described in the previous paragraph. Thus, it is possible to construct a composite geodesic structure with longitudinal, helical, and circumferential elements, yet maintain high structural efficiency within the elements.

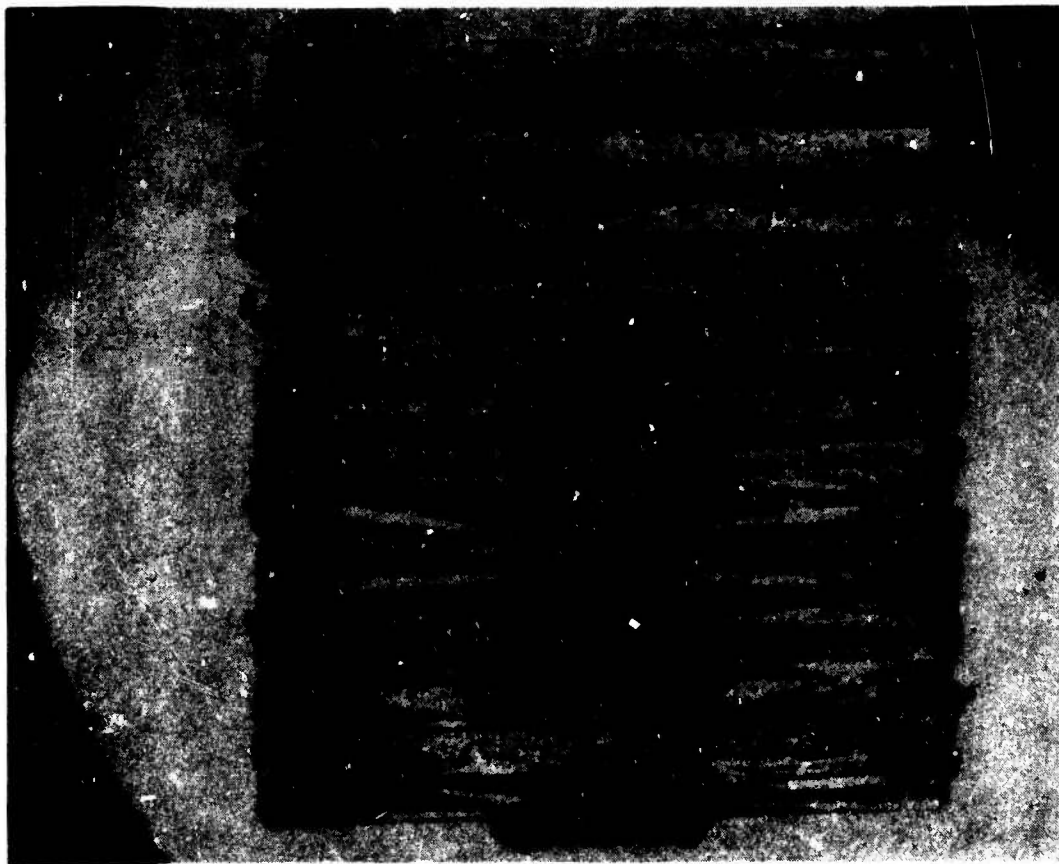


Figure 2. Cross Section of a Typical Two-Element Intersection.

Reproduced from
best available copy.



PARAMETRIC ANALYSIS

The design of a geodesic plate is analogous to the design of a laminated composite plate. Physical and mechanical properties of the plate are a function of constituent materials and element orientation, size, and spacing. A parametric analysis was conducted to determine the effects of these variables on the mechanical properties of geodesic plates. The basic system of equations used for the computerized analysis of these variables is outlined in this section.

For derivation of equations used to predict the structural behavior of a geodesic plate, the following basic assumptions pertaining to the analysis of anisotropic plates were made:⁷

- a. All elements are of equal thickness, and the axis of material symmetry of an element coincides with the midplane of the plate.
- b. The in-plane bending stiffness and torsional stiffness of each element were neglected since, for the element geometries considered in this study, the axial stiffness and the out-of-plane bending stiffness of the element were much greater than its in-plane bending stiffness and torsional stiffness.
- c. The thickness of the plate is smaller than its length or width.
- d. In-plane strains are small compared to unity.
- e. Transverse normal strain is negligible.
- f. Each element obeys Hooke's law.

The constitutive equation for anisotropic plates can be written in an abbreviated form as a partitioned matrix equation, as follows:

$$\begin{bmatrix} N \\ M \end{bmatrix} = \begin{bmatrix} A & B \\ B & D \end{bmatrix} \begin{bmatrix} \epsilon \\ \chi \end{bmatrix} \quad (1)$$

Assumption (a) eliminates coupling between extensional deformation and bending deformation, and thus the constitutive equation may be reduced to the following:

$$\begin{bmatrix} N \end{bmatrix} = \begin{bmatrix} A \end{bmatrix} \begin{bmatrix} \epsilon \end{bmatrix} \quad (2)$$

$$\begin{bmatrix} M \end{bmatrix} = \begin{bmatrix} D \end{bmatrix} \begin{bmatrix} \chi \end{bmatrix} \quad (3)$$

The stiffness coefficients of Equations (2) and (3) are obtained by imposing on a typical section of the plate, one at a time, the deformation equations and then determining the corresponding stress resultants for a unit value of deformation.

The general equation for the in-plane stiffness matrix takes the form

$$[A] = \sum_{k=1}^n [C'_{ij}]^{(k)} \quad (4)$$

Here $[C'_{ij}]^{(k)}$ is the stiffness matrix associated with the extensional deformation of an element referred to the reference axis of the plate. When referred to the element axis of symmetry, this matrix is written as follows:

$$[C_{ij}]^{(k)} = \begin{bmatrix} Ebt/P & 0 & 0 \\ 0 & 0 & 0 \\ 0 & 0 & 0 \end{bmatrix}^{(k)} \quad (5)$$

The element stress-strain relations are transformed from the element axis to the reference axis of the plate with the following equation:

$$[C'_{ij}] = [T]^{-1} [C_{ij}] [T] \quad (6)$$

where $[T]$ is the transformation matrix given by

$$[T] = \begin{bmatrix} m^2 & n^2 & 2mn \\ n^2 & m^2 & -2mn \\ -mn & mn & m^2 - n^2 \end{bmatrix} \quad (7)$$

where $m = \cos \phi$, $n = \sin \phi$.

The flexural stiffness matrix is developed in a similar manner:

$$[D] = \sum_{k=1}^n [K'_{ij}]^{(k)} \quad (8)$$

and the flexural deformation of an element referred to the element axis of symmetry is written as follows:

$$[K_{ij}]^{(k)} = \begin{bmatrix} Ebt^3/12P & 0 & 0 \\ 0 & 0 & 0 \\ 0 & 0 & 0 \end{bmatrix}^{(k)} \quad (9)$$

The average plate elastic moduli may be obtained from the components of the plate compliance matrix A^* .

$$\begin{bmatrix} A_{ij}^* \end{bmatrix} = \begin{bmatrix} A_{ij}/t \end{bmatrix}^{-1} \quad (10)$$

The average plate elastic constants are given by the following:

$$\begin{aligned} E_x &= 1/A_{11}^* \\ E_y &= 1/A_{22}^* \\ G_{xy} &= 1/A_{33}^* \\ \mu_{xy} &= -A_{12}^*/A_{11}^* \end{aligned} \quad (11)$$

For a given loading condition, the strain in the elements coincident with the reference axis of the plate is determined by inversion of Equation (2):

$$[\epsilon] = [A]^{-1} [N] \quad (12)$$

The strain in elements oriented at $\pm\phi$ to the reference axis of the plate is determined by use of the transformation matrix T .

Plate strength was determined by evaluation of the strain level within the various elements. Since the analysis was linear elastic behavior, failure of the plate was assumed to occur when the strain level in one of the elements exceeded its allowable.

A computer program was written using the foregoing equations to enable the rapid computation of the mechanical properties of geodesic plates for design purposes. The program is described in the appendix to this report.

Aside from constituent materials, element orientation and the amount of material at each orientation within the plate have the most effect upon the mechanical characteristics of geodesic plates. The first family of geodesic plates investigated was constructed with elements oriented at $\pm\phi$ and 90° as shown in the schematic in Figure 3.

The results of parametric analysis were nondimensionalized by dividing the specific stiffness or strength of the plate by the specific stiffness or strength of the elements within the plate. The effective density of the plate is defined as the total weight of the elements within a typical cell divided by the total volume of the cell (P_x by P_y by t).

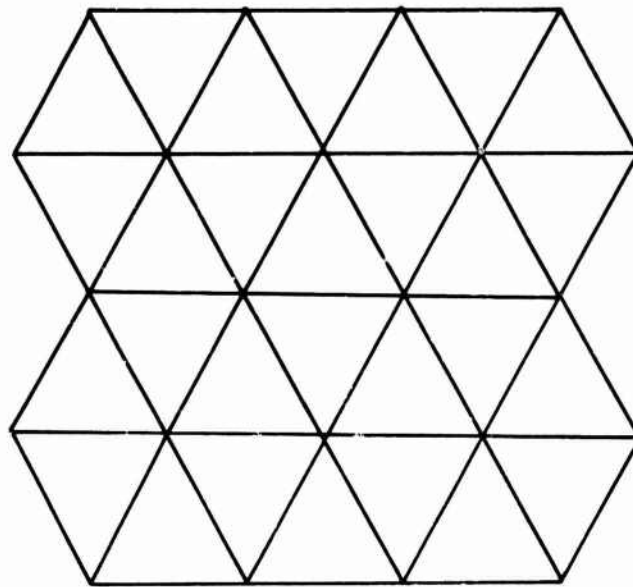


Figure 3. Schematic of $\pm \phi, 90^\circ$ Element Pattern.

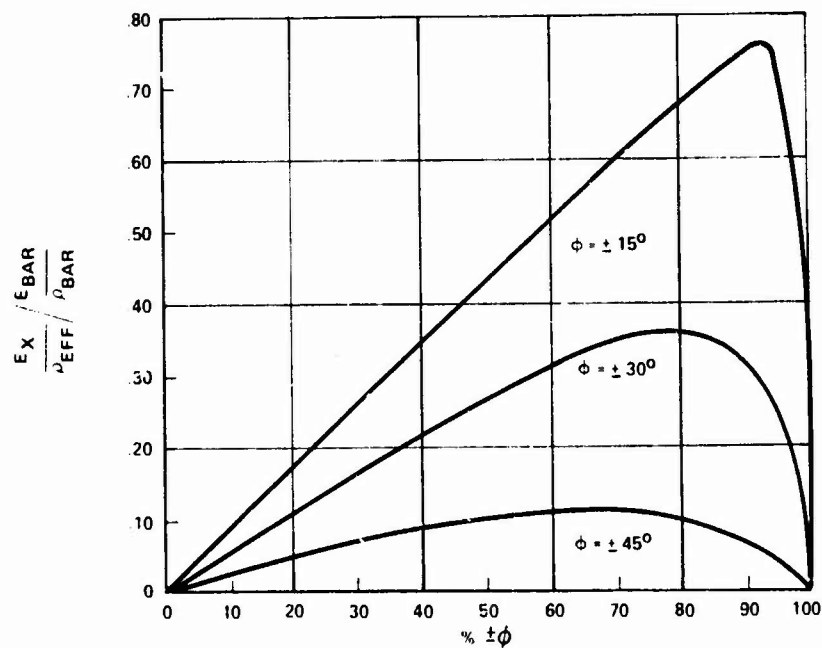


Figure 4. Axial Stiffness Parameter for Panels With Elements at $\pm \phi, 90^\circ$.

Axial stiffness and strength of geodesic plates composed of elements oriented at $\pm\phi$ and 90° are plotted as functions of the volumetric percentage of material at $\pm\phi$ in Figures 4 and 5, respectively.

Inspection of the curves in Figures 4 and 5 reveals two significant factors. First, as with laminated composites, the closer the orientation angle is to the longitudinal axis, the greater the longitudinal strength or stiffness. Second, as the percentage of $\pm\phi$ material increases, both stiffness and strength of the plate increase until a point is reached wherein insufficient material exists at 90° to inhibit lateral deformation and react lateral loading.

The effect of element orientation angle and the volumetric percentage of $\pm\phi$ material on the in-plane shear stiffness of geodesic plates constructed with elements at $\pm\phi$ and 90° are shown in Figure 6. Note that shear stiffness increases linearly with the amount of $\pm\phi$ material, and that the $\pm 45^\circ$ orientation yields the greatest shear modulus of the orientations investigated.

Stiffness and strength of a plate can be tailored to meet structural requirements by selection of element orientation angle and size. For application to a rotor blade, the $\pm 30^\circ$ orientation was selected for the helical elements because it offered the best combination of torsional stiffness and longitudinal stiffness and strength.

Increased design flexibility is obtained by addition of 0° elements (Figure 7) to the $\pm 30^\circ$, 90° system of elements. The axial modulus, axial strength and in-plane shear stiffness of the family of plates constructed with elements oriented at 0° , $\pm 30^\circ$, and 90° are shown in Figures 8, 9 and 10 respectively. The proportion of elements in each direction may be selected to yield the plate strength and stiffness required to meet the design criteria.

The material properties of the reinforcements considered for the geodesic structure of the blade are listed in Table 1.

TABLE 1. FIBER MATERIAL PROPERTIES				
Fiber	Tensile Modulus (10^6 PSI)	Tensile Strength (10^3 PSI)	Density ($\text{lb}/\text{in.}^3$)	Reference
Intermediate-Strength Graphite	34	325	.061	8
High-Modulus Graphite	53	300	.068	8
Organic Kevlar 49	19	400	.053	9
"S" Glass	12.6	535	.090	10

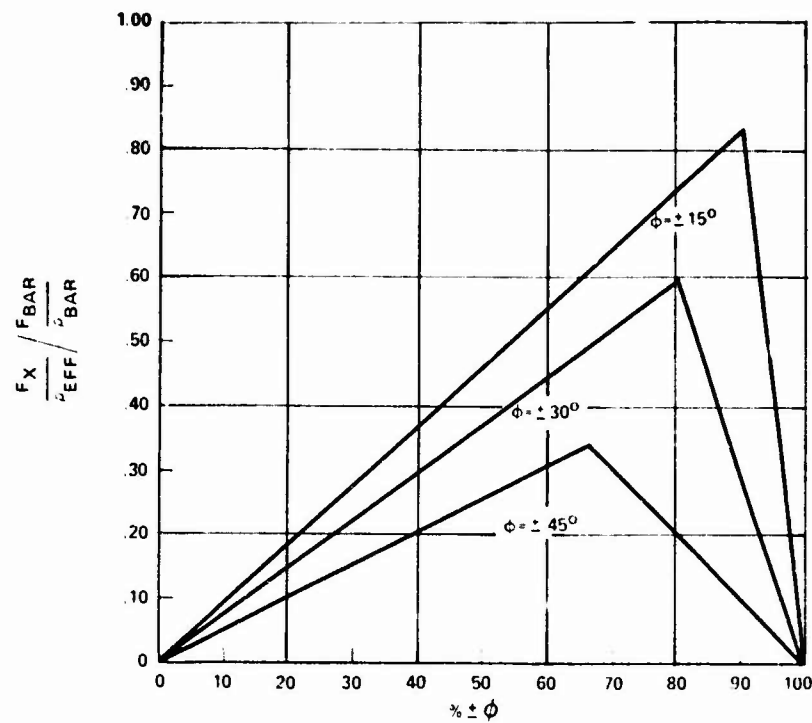


Figure 5. Axial Strength Parameter for Panels With Elements at $\pm\phi, 90^\circ$.

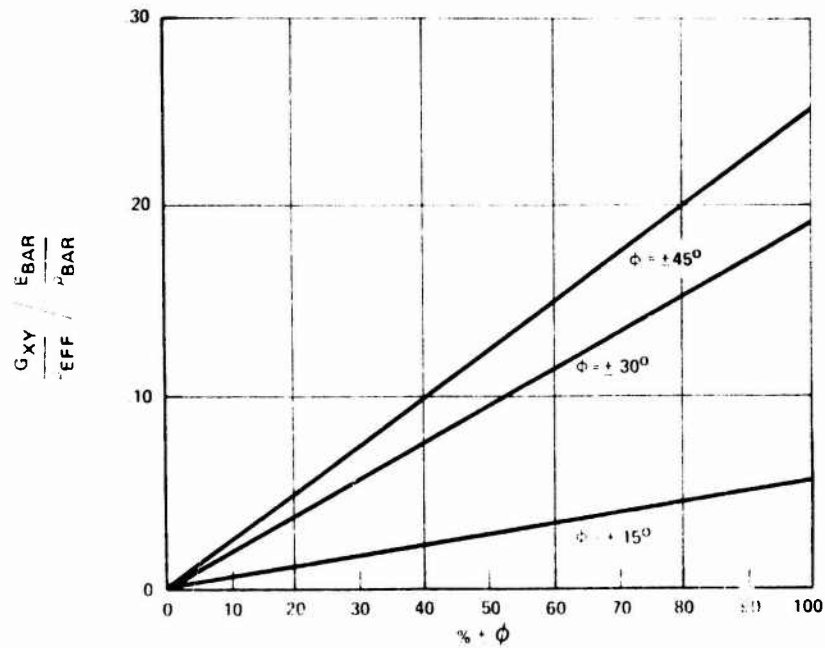


Figure 6. Shear Stiffness Parameter for Panels With Elements at $\pm\phi, 90^\circ$.

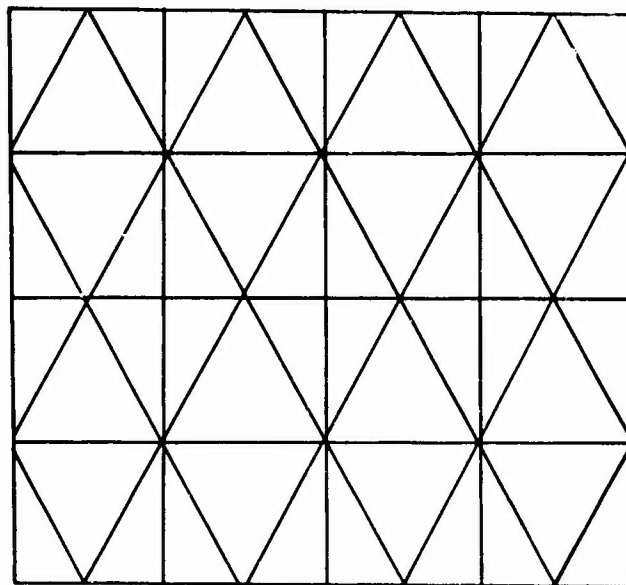


Figure 7. Schematic of 0° , $\pm 30^\circ$, 90° Element Pattern.

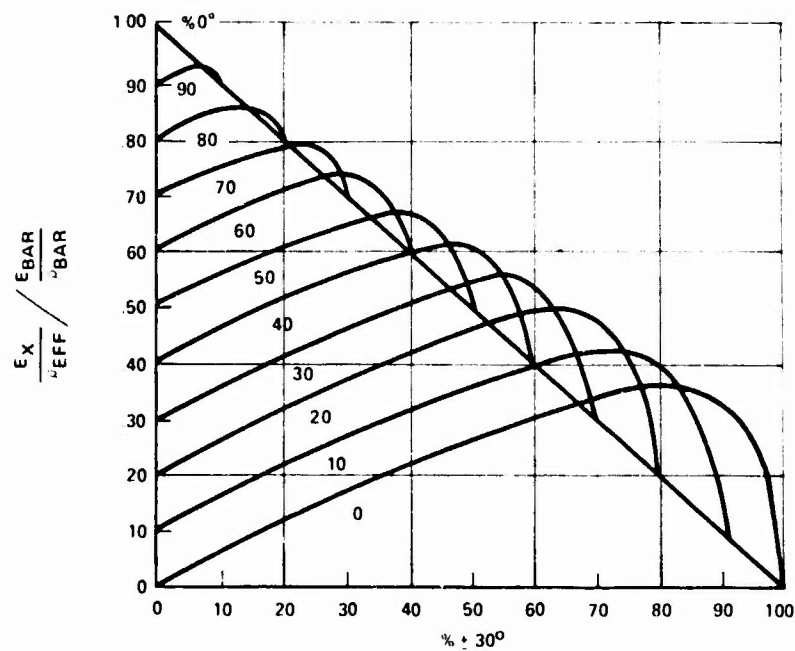


Figure 8. Axial Stiffness Parameter for Panels With Elements at 0° , $\pm 30^\circ$, 90° .

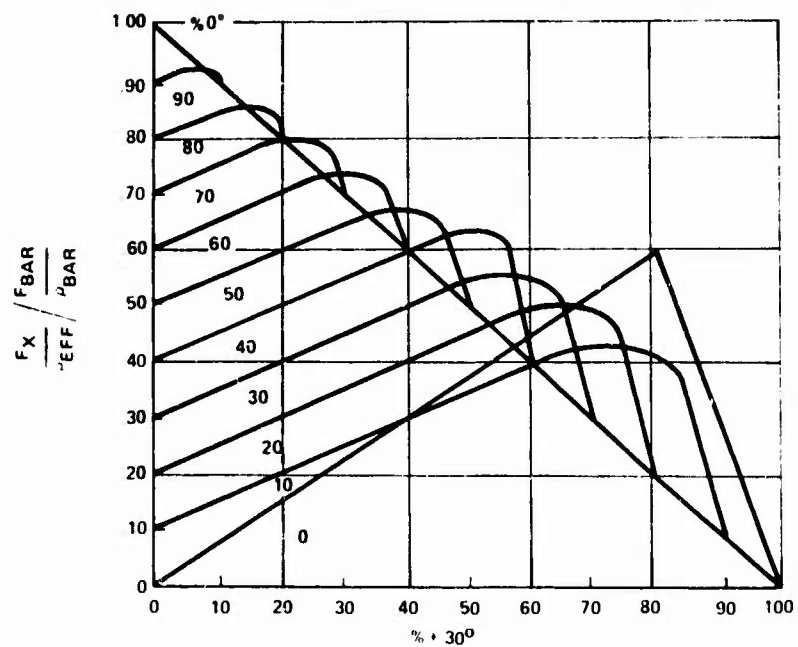


Figure 9. Axial Strength Parameter for Panels With Elements at 0° , $\pm 30^\circ$, 90° .

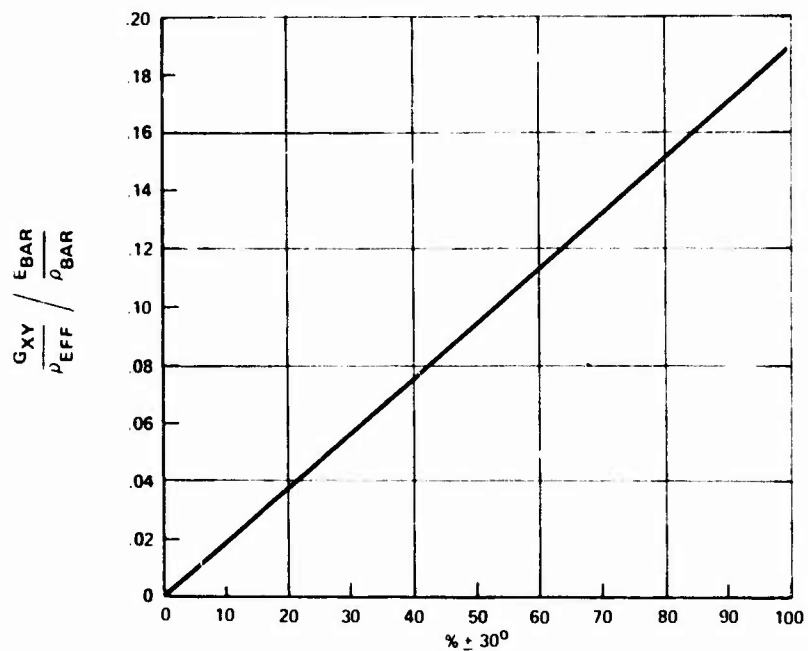


Figure 10. Shear Stiffness Parameter for Panels With Elements at 0° , $\pm 30^\circ$, 90° .

Properties of Table 1 and micromechanics were used to determine the axial stiffness and strength of unidirectional composites containing a fiber volume of 50%. The axial modulus and strength of a bar were calculated as follows:

$$E_{\text{BAR}} = E_f V_f + (1-V_f) E_m \quad (13)$$

$$F_{\text{BAR}} = F_f V_f + (1-V_f) F_m \quad (14)$$

where V_f is the volume of fibers within the bar, and E_f , F_f and E_m , F_m are the modulus and strength of the fiber and matrix material respectively.

The strengths of geodesic panels with all elements constructed of the same material and of panels wherein the $\pm 30^\circ$ elements and 90° elements are of differing materials (hybrid construction) were predicted. The specific axial stiffness and axial strength of these panels are plotted versus volumetric percentage of $\pm 30^\circ$ materials for panels constructed with elements at $\pm 30^\circ$ and 90° in Figures 11 and 12. It is interesting to note that hybridization can cause a shift in the amount of 30° material required for optimum strength and stiffness. Thus hybridization offers additional design flexibility for arriving at a minimum weight to satisfy specific stiffnesses and loads. By adding still another set of variables, types of material and amount of material in 0° elements, even greater design flexibility is added.

Specific material combinations and proportions of $\pm 30^\circ$ and 90° elements were selected from the combinations presented in Figure 11 and combined with 0° elements of various materials to construct the curves presented in Figure 13. Here the specific axial stiffness of the panel is plotted as a function of the volumetric percentage of the amount of $\pm 30^\circ$, 90° material in the panel.

Hybridization offers possibilities of trading specific stiffness for specific strength and adding design flexibility to the system. However, within the scope of this research program, it was considered that hybridization could cause complications in interpretation of the structural test data. Thus, Thornel 300/epoxy geodesic construction having elements oriented at 0° , $\pm 30^\circ$, 90° was selected for further investigation for application to rotor blades.

DAMAGE TOLERANCE

Geodesic construction was selected as the primary design concept for a damage-tolerant rotor blade because of the crack insensitive nature of this structure. An investigation of the structural response of four gridwork geometries containing ballistic damage of various sizes was conducted using the NASA Structural Analysis (NASTRAN) finite element computer program.

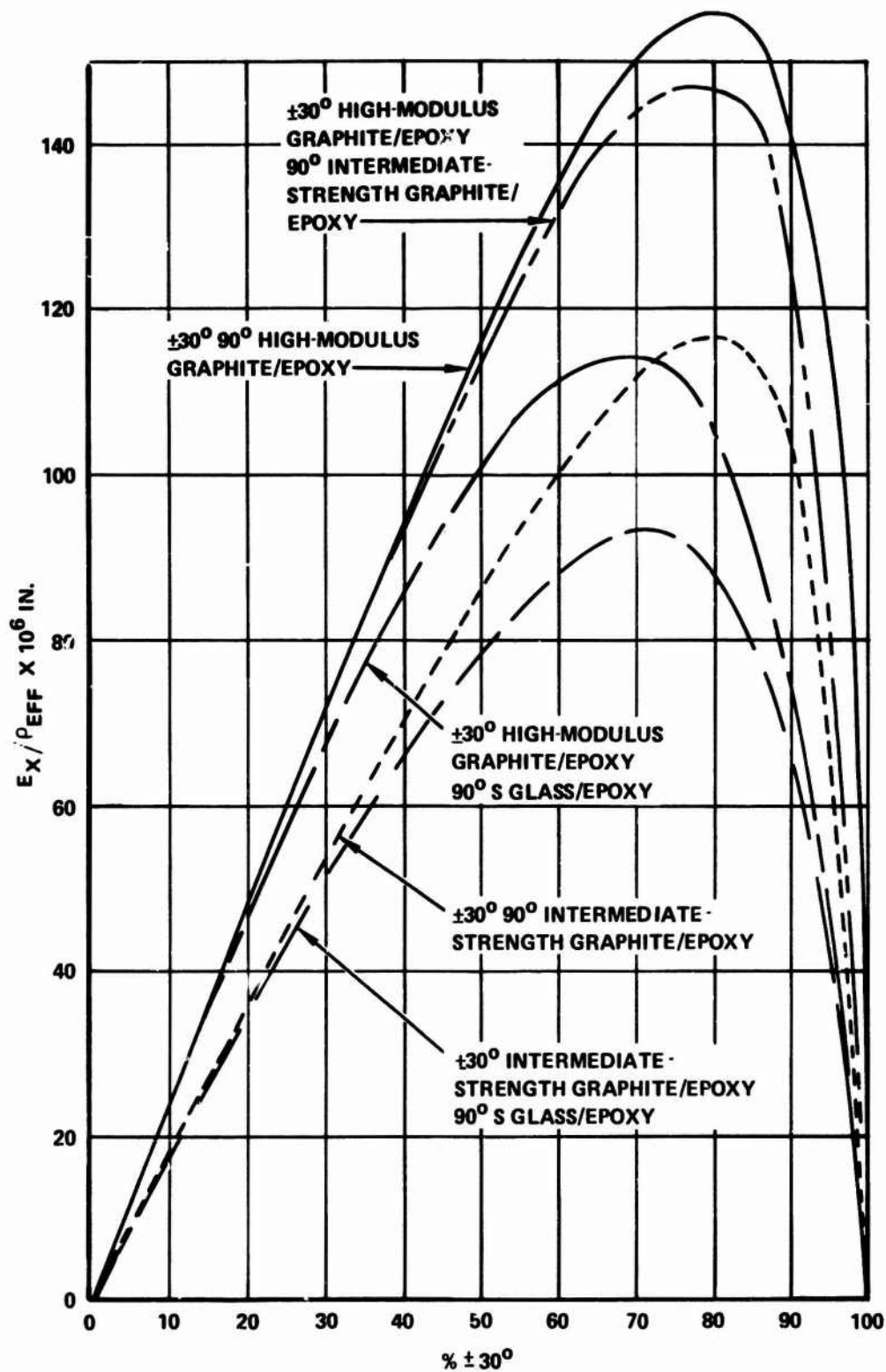


Figure 11. Specific Axial Stiffness of $\pm 30^\circ$, 90° Panels.

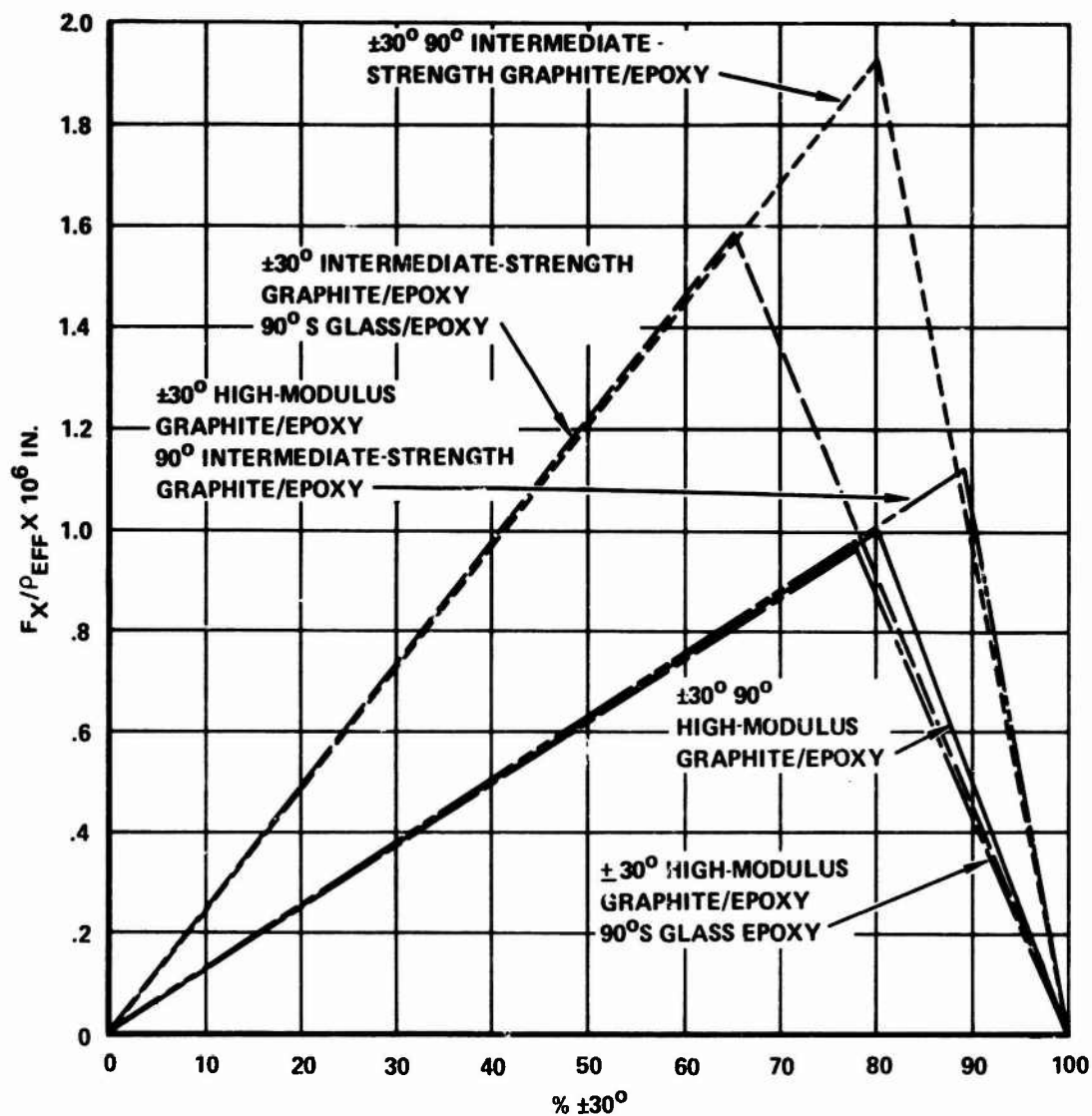


Figure 12. Specific Axial Strength of $\pm 30^\circ$, 90° Panels.

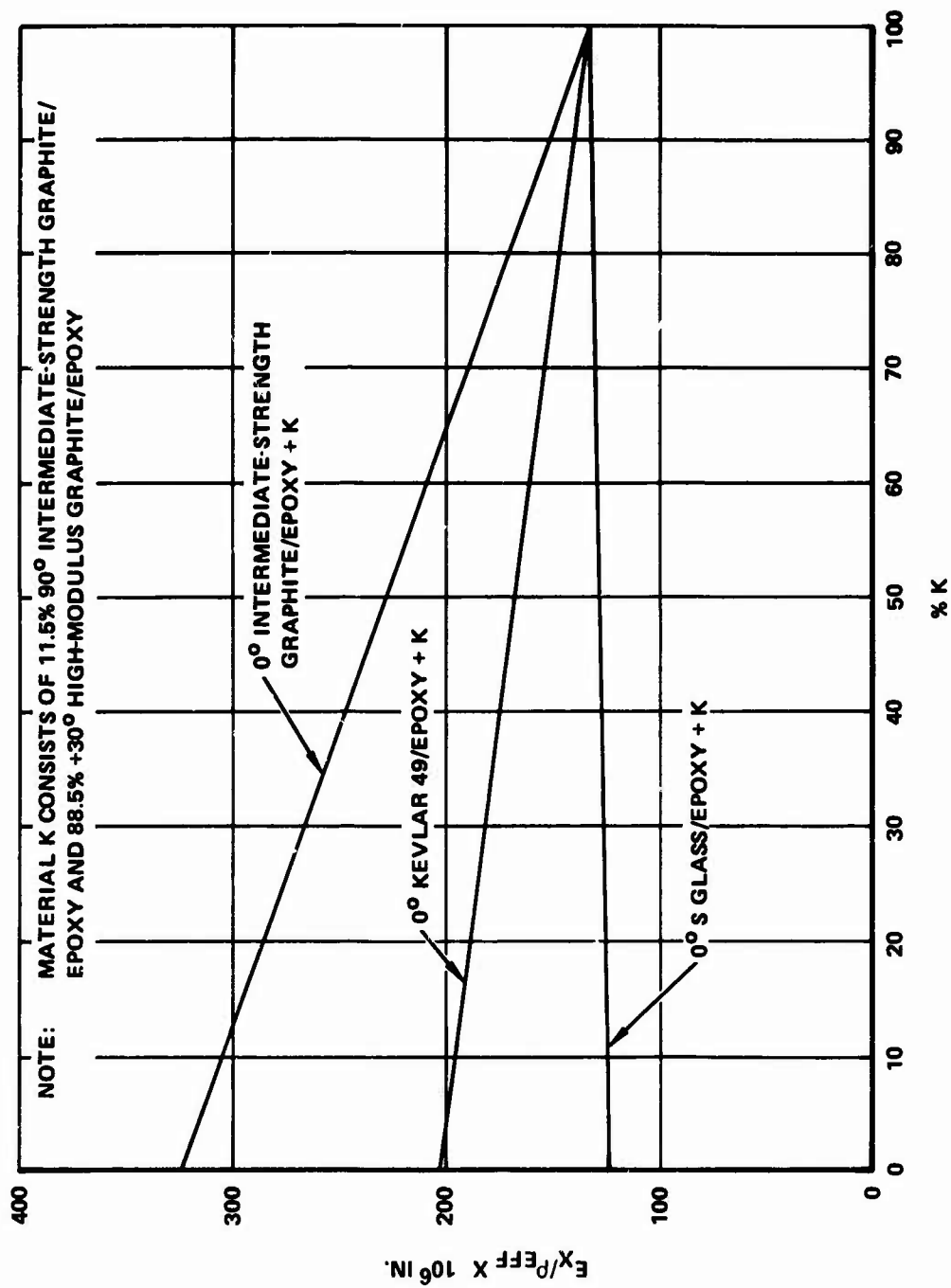


Figure 13. Specific Axial Stiffness of 0° ±30°, 90° Panels.

Consistent with the assumptions made for the parametric analysis, the panels were considered as two-dimensional plates and the elements modeled as rods capable of carrying tension or compression loads. As shown in Figure 14, the panels were symmetrical about both axes; thus, analysis of one quadrant sufficed. Element stress levels within a panel subjected to tensile loading were computed before and after ballistic damage.

The stress-strain behavior of an element was considered perfectly elastic to failure. Panel failure was assumed to occur when the stress level within any element reached its rupture strength. Further redistribution of the internal loads was not considered because of the preliminary nature of this study.

A description of the configurations analyzed and a summary of the results obtained are given in Table 2. For the configurations investigated, it appeared that the addition of 0° elements did not significantly increase damage tolerance. In fact, in the last case ($b_x = 3b_y$), damage tolerance is lowered. However, the method of analysis^x was conservative because it was linear elastic and allowed for failure of only one element.

A comparison of the predicted residual strength for a geodesic panel with 66.67% $+30^\circ$ elements and 33.33% 90° elements (isogrid) and test data on laminated composite panels is shown in Figure 15.

Based on these limited data, it appears that the geodesic panel investigated has damage tolerance superior to laminated composites for hole diameter to width ratios less than 30%. Above this ratio the test results for the quasi-isotropic laminated composite and predictions for geodesic composite panels are identical.

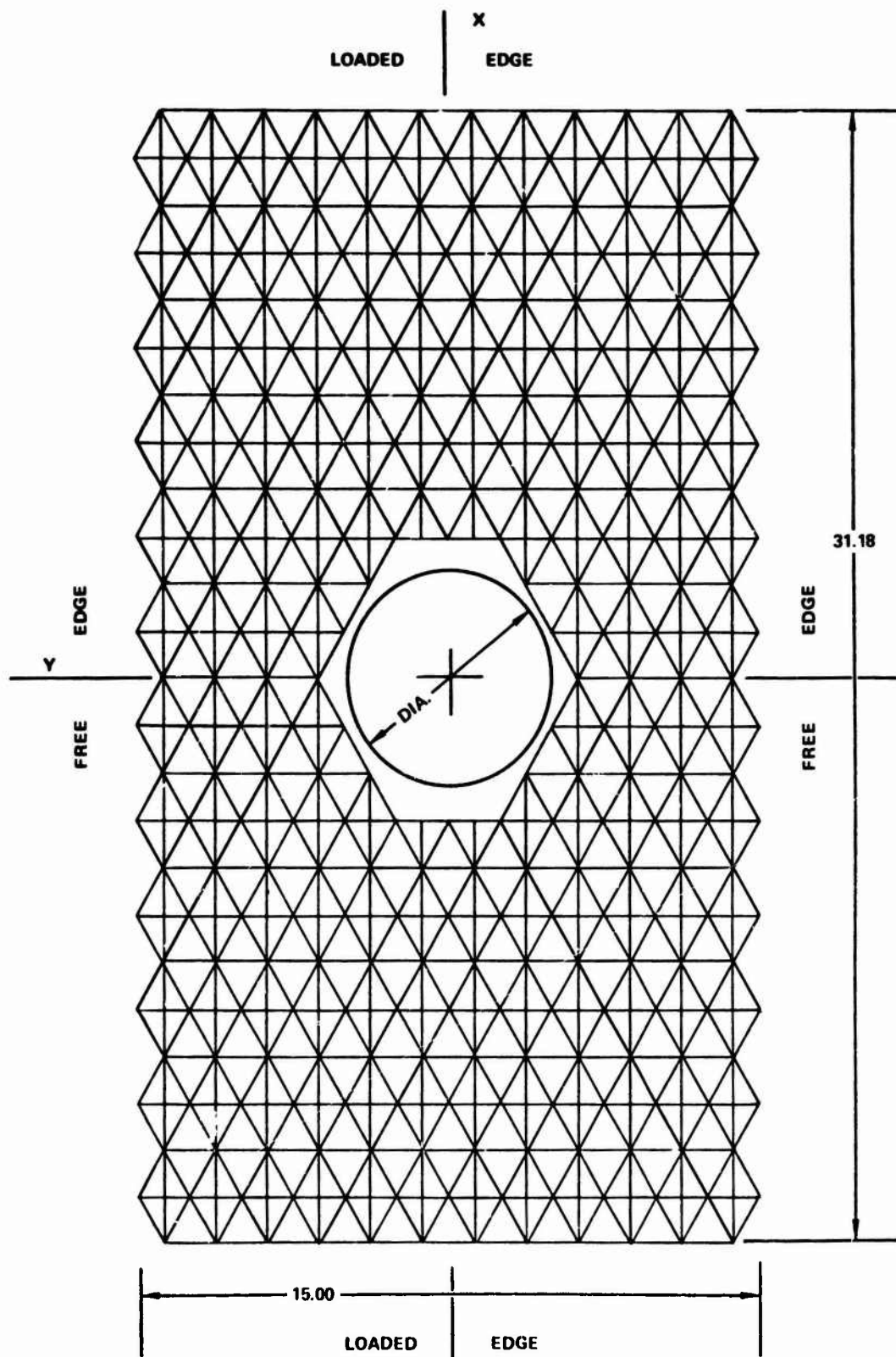
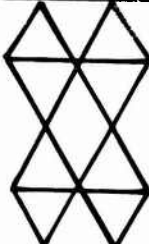
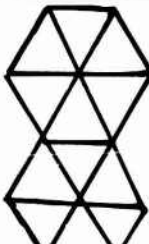
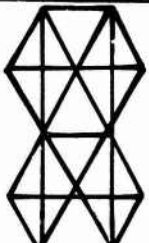
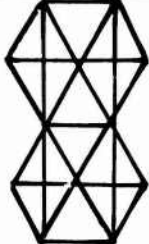
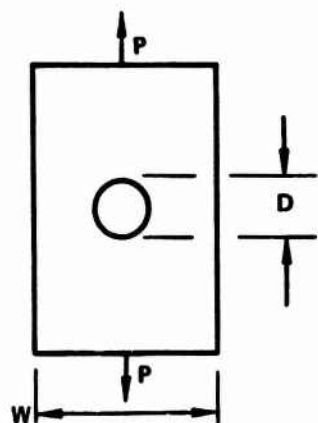


Figure 14. Schematic of a Geodesic Plate Containing Ballistic Damage.

TABLE 2. PREDICTED DAMAGE TOLERANCE OF GEODESIC PLATES

Configuration	Damage Diameter Plate Width	Damaged Strength Undamaged Strength
 $P_x = 1.50 \text{ in.}$ $b_y = b_{PHI}$ $\phi = \pm 30^\circ$.3334	.40
 $P_x = 1.50 \text{ in.}$ $b_y = b_{PHI}$ $\phi = \pm 30^\circ$.1667 .3334 .5000	.66 .45 .32
 $P_x = 1.50 \text{ in.}$ $b_x = b_y = b_{PHI}$ $\phi = \pm 30^\circ$.1667 .3334 .5000	.67 .46 .33
 $P_x = 1.50 \text{ in.}$ $b_y = b_{PHI}$ $b_x = 3b_y$ $\phi = \pm 30^\circ$.3334	.36



BORON/EPOXY

- ⊖ $(\pm 45, 0_2, 0)_s$
- $(\pm 45, \pm 45)_s$
- ⊖ $(0, 90, 0, 90)_s$
- $(0, \pm 45, 0, \overline{90})_s$

GRAPHITE/EPOXY

- $(0, \pm 45, 0, \overline{90})_s$

GLASS/EPOXY

- ⊕ $(0, \pm 45, 0, \overline{90})_s$

DATA FROM REFERENCE 11

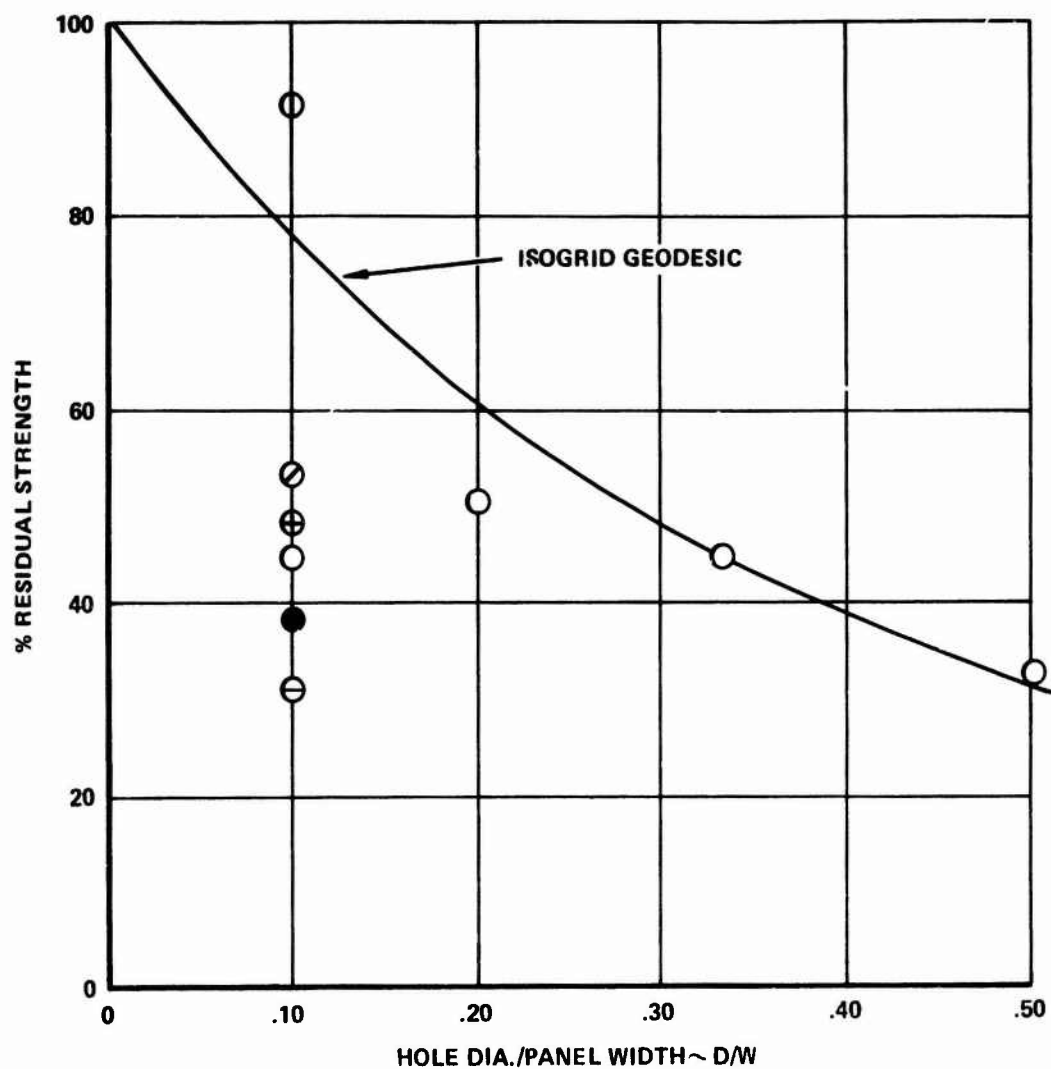


Figure 15. Residual Strength for a Panel With 66.7% $\pm 30^\circ$ and 33.33% 90° Elements.

SPECIMEN FABRICATION AND TESTS

FABRICATION AND TEST PLAN

A specimen fabrication and test program was conducted to verify analytical predictions and serve as a basis for design. It was decided to fabricate beam specimens having a configuration typical of a helicopter main rotor blade spar rather than to test coupons which were fabricated under carefully controlled conditions using specialized tooling.

Coupons were cut from the surfaces of the beams and statically tested to determine strength and stiffness of basic elements and thus provide a design tool for predicting full-scale behavior.

TOOLING AND FABRICATION

The tooling employed in the fabrication of composite geodesic structures was based on the concept of producing composite tubular components by applying the laminating pressure to the inside surface of the mandrel upon which the structure was wound and reacting this pressure on the outside with a female die. This technique enabled close tolerances to be held on surface contour and subsequently reduced the number of finishing operations.

A mandrel was designed to serve as a form on which the structure was laid up and to support the elements during the pressure application and debulking phase to preclude collapse and distortion. Since the mandrel was pressurized during the cure cycle, it was constructed of rubber to transmit pressure uniformly throughout the component.

The rubber mandrel was cast in a tubular configuration with the geodesic pattern inscribed on its outer surface. A rigid support was used to hold the rubber mandrel during the winding operation. Fittings with protruding pins attached to the ends of the mandrel support effected a change in direction of the fibers without making it necessary to wrap the fibers over the end of the mandrel. The tools used for the beam specimens are shown in Figure 16. The geodesic structure was laid up on the mandrel using resin impregnated yarn. After the structure was wound, the mandrel assembly was transferred to a set of female tools, the end fittings and mandrel support were removed, and the rubber bag was sealed to the female tools. This entire assembly was then transferred to an autoclave and cured.

Four beam specimens were fabricated, one of which is shown in Figure 17. The specimen was 9.25 inches wide, 3 inches deep and 52 inches long, with a grid pattern composed of elements oriented at 0° , $\pm 30^{\circ}$ and 90° .

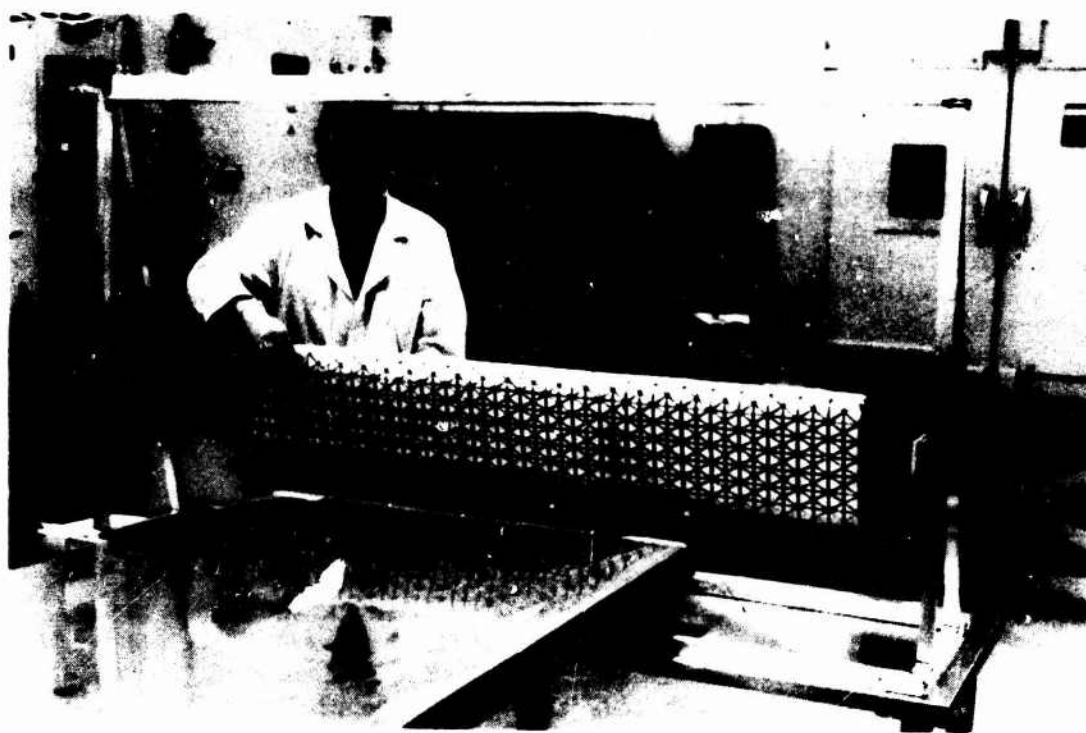


Figure 16. Tooling for Beam Specimens.

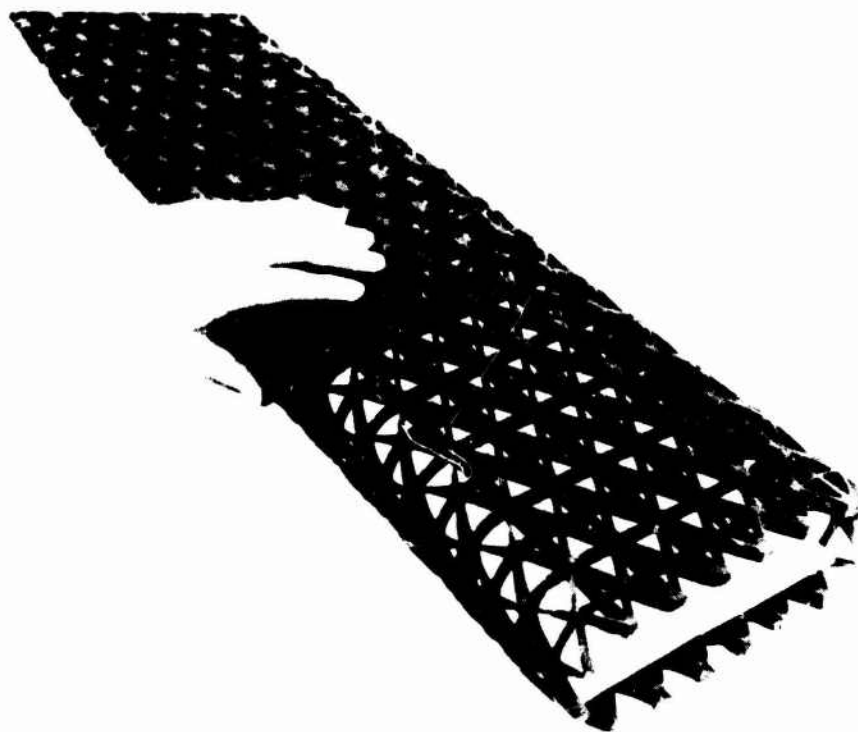


Figure 17. Graphite/Epoxy Beam Specimen.

A typical element has dimensions of 0.5 inch deep by 0.1 inch wide, and the spacing of the 0° elements is 1.25 inches. A Thornel 300/APCO 434 wet system was used to construct the beam specimens.

It is believed that the hand-winding procedures used to fabricate the beam specimens resulted in a nonuniform distribution of the fibers within the elements and poor fiber collimation. Inability to maintain the correct yarn tension during the winding operation caused the mandrel cavities to fill prematurely, and thus the specimens had a lower fiber volume than anticipated. Subsequent improvement in the hand-winding techniques resulted in the fabrication of better quality specimens. However, these problems may be eliminated by use of a specially modified filament-winding machine to promote better fiber collimation and uniformity within the element.

TEST RESULTS

Tensile tests were conducted on three coupon configurations: single elements, two- and three-cell-wide plates, and full beams.

The single-element coupons were machined from the longitudinal (0°) elements of two beam specimens. Table 3 provides a comparison of the test results and analytical predictions. A typical load-deflection curve for a single-element specimen is shown in Figure 18. Note that the behavior is linear to failure. Investigation of the failed specimens indicates that the fractures originated at the intersection of the 0° , $+30^\circ$ and 90° elements.

Both two- and three-cell-wide configurations of plate specimens were machined from the surfaces of the beam specimens. A typical three-cell-wide specimen is shown in Figure 19, and a failed specimen is shown in Figure 20. Table 4 presents the test results of static tensile tests on the plate specimens.

End fittings were mounted on two beam specimens, and these were tested in tension. A typical specimen mounted in the test machine is shown in Figure 21. One specimen was tested to failure; the other was proof tested. The test results are shown in Table 5. The load-strain behavior of the elements within the beam is shown in Figure 22.

The test results presented in Tables 3, 4 and 5 indicate that the geodesic construction did not behave as predicted. All specimens failed at stress levels below the predicted strength, and also the specimens demonstrated slightly less stiffness than predicted.

It was postulated that wrinkling of fiber bundles in nodal regions and nonuniform yarn tension caused by hand-winding were responsible for discrepancies in the predicted strength and stiffness of the specimens.

TABLE 3. SINGLE-ELEMENT SPECIMEN TEST RESULTS									
Spec No.	Cross Section Area (in. ²)	Fiber Volume (%)	Predicted Modulus** (10 ⁶ psi)	Predicted Strength** (10 ³ psi)	Measured Failure Load (10 ³ lb)	Measured Failure Strength (10 ³ psi)	Measured Modulus (10 ⁶ psi)	Measured Failure Strain (10 ⁻³ in./in.)	Predicted Strength Actual Strength
1-5-1	.0313	44.2	15.3	148.9	2.88	92.01	*	*	1.62
1-5-2	.0393	49.4	17.0	165.3	2.88	73.28	15.3	*	2.26
1-5-3	.0329	38.8	13.5	131.9	2.78	84.50	14.4	*	1.56
1-5-4	.0377	40.4	14.0	136.3	3.32	88.06	12.6	*	1.55
3-5-1	.0461	30.7	10.8	106.4	3.31	71.80	9.53	7.50	1.48

4

*Not recorded.

**These predictions are based on measured fiber volumes and the analyses/techniques derived on pages 15 through 23 using equations (1) through (14).

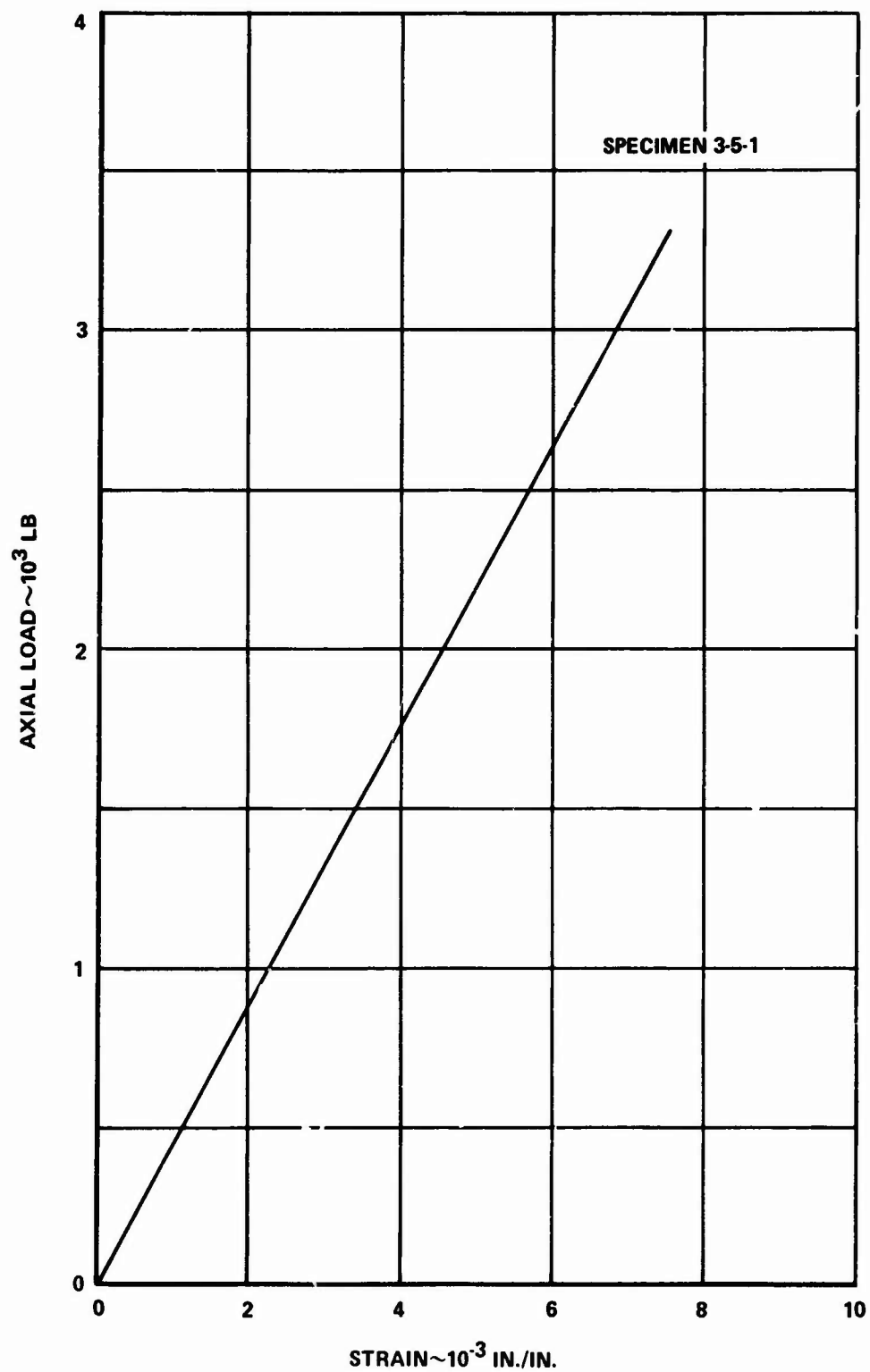


Figure 18. Load Strain Curve for a Single-Element Specimen.

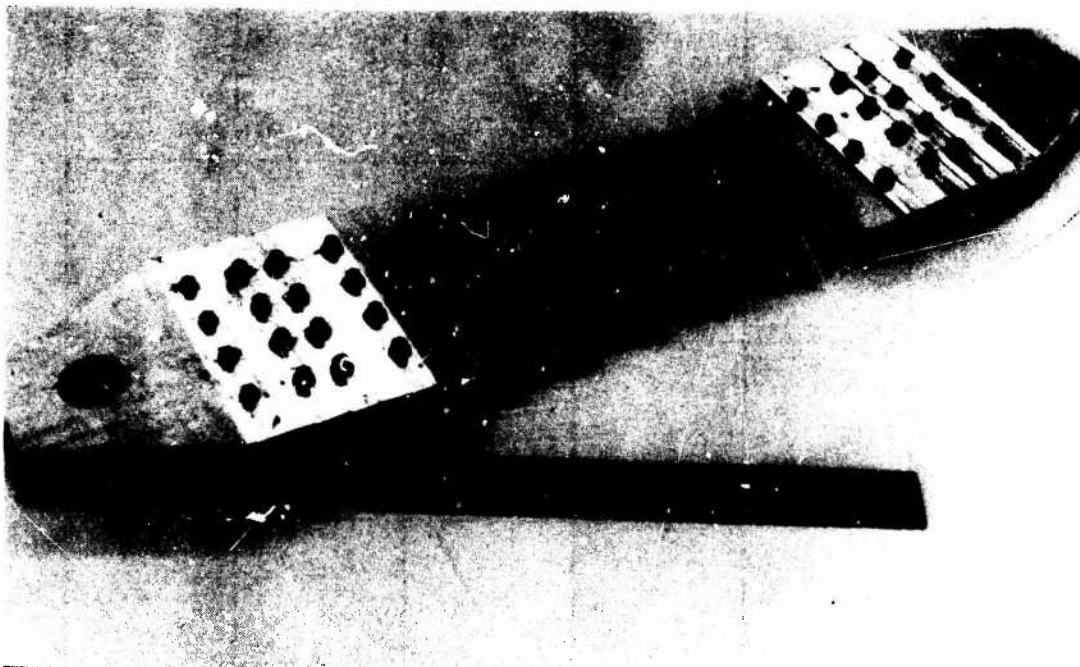


Figure 19. Three-Cell-Wide Plate Specimen.



Figure 20. Failed Plate Specimen.

TABLE 4. PLATE SPECIMEN TEST RESULTS

Spec No.	Description	Size (in.)	Average Element Size (in.)	Average Element Fiber Vol. (%)	Predicted Modulus** (10^6 psi)	Predicted Strength** (10^3 psi)	Actual Modulus (10^6 psi)	Actual Strength (10^3 psi)	Predicted Strength / Actual Strength
1-1-1	2-CELL	2.50 x .431	.431 x .090	40.9	2.2	21.4	*	10.20	2.10
1-1-2	2-CELL	2.50 x .431	.431 x .090	40.9	2.2	21.4	*	11.02	1.94
1-3-1	3-CELL	3.75 x .431	.431 x .090	40.9	2.2	21.4	*	9.51	2.25
1-3-2	3-CELL	3.75 x .431	.431 x .090	40.9	2.2	21.4	*	9.01	2.38
3-1-1	3-CELL	3.75 x .495	.454 x .094	33.4	1.9	17.0	1.83	9.25	1.84

* Not recorded.

** Same note as on page 34.

TABLE 5. BEAM SPECIMEN TEST RESULTS

Spec No.	Average Element Size (in.)	Average Fiber Volume (%)	Predicted Stiffness EA** (10^6 lb)	Predicted Rupture Load** (10^3 lb)	Actual Stiffness EA (10^6 lb)	Actual Rupture Load (10^3 lb)	Predicted Strength / Actual Strength
3	.454 x .094	33.4	14.2	*	13.3	*	*
4	.495 x .116	24.8	16.1	154.0	12.5	84.1	1.83

* Specimen No. 3 not tested to failure

** Same note as on page 34.



Figure 21. Test Setup for Beam Specimen.

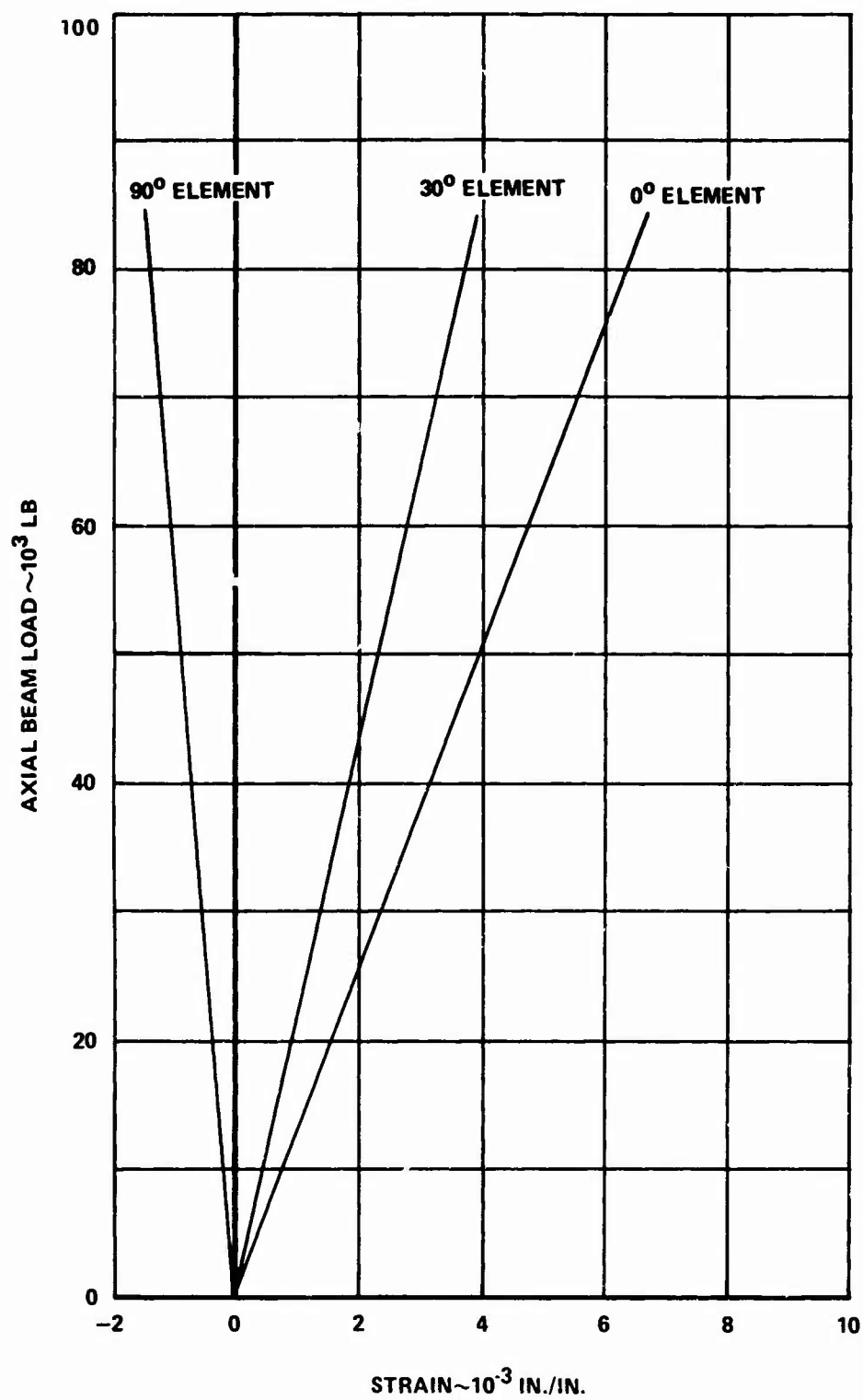


Figure 22. Load-Strain Curves for Beam Specimen Elements.

Further static and fatigue testing of composite geodesic specimens should be conducted. The effects of geometrical variables, such as the number of elements that intersect at a node, and fabrication variables, such as winding tension and curing pressure on mechanical properties, should be experimentally investigated.

ROTOR BLADE

DESIGN

A preliminary design study of a helicopter main rotor blade was conducted using composite material geodesic structure. Blade design criteria stipulated that the same airfoil geometry be used, and that stiffness and weight distributions for the geodesic blade be approximately the same as for an original metallic blade.

The original rotor system investigated is a four-bladed system having a radius of 25.617 feet with a blade chord of 28 inches. Rotor blade thickness varies from 6% at the tip to 12% at the centerline of rotation.

The conceptual design of the geodesic rotor blade is shown in Figure 23. Important features of the design are described in the following sections.

Geodesic Spar

The primary structural element within the blade is the geodesic box spar constructed of Thornel 300/epoxy. This spar has helical elements oriented at $+37^{\circ}$ and $+34^{\circ}$ and circumferential elements at $+85.5^{\circ}$. Longitudinal, 0° , elements are located in the leading-edge and trailing-edge sections of the spar to tailor the flap and in-plane stiffnesses. The unsymmetric element orientation was selected to allow the circumferential elements to be wrapped as a continuous helix. Note that the pattern contains two-element and three-element intersections only. Four-element intersections were eliminated to allow greater fiber volumes in the elements and to reduce the wrinkling of the fiber bundles in the nodal regions.

In comparison to a conventional rotor blade where the primary spar is approximately 30% of the chord, the geodesic box covers 57% of the blade chord. This approach was taken to guarantee that a minimum amount of material is removed due to ballistic damage. The maximum width of the spar was dictated by the requirement of a 0.25-inch minimum radius on the circumferential graphite/epoxy element.

The stiffness distribution of the blade is tailored by varying the thickness of the geodesic elements linearly from 0.378 inch at the tip to 0.56 inch at Rotor Station 140 to 0.66 inch at the root end, and by the addition of longitudinal elements at Rotor Station 140 and Rotor Station 120.

Root End Attachment

A lug-type root end attachment was designed for the blade because it offered greater structural efficiency and was more compatible with the manufacturing process than a shear type attachment. The lug locations and sizes were designed to insure proper attachment to the movable hub.

Tip Weight

The geodesic elements at the blade tip wrap around a tip weight retention bar. This bar contains studs to which the tip weight housing is attached.

Antinode Weight

The antinode weight consists of a mass of tungsten-filled epoxy which would be potted in place after the cure of the basic geodesic box.

Balance Bar

A nonstructural balance bar was designed which consists of brass segments bonded to the nose skin.

Trailing-Edge Cell

The trailing-edge cell of the blade is constructed of fiberglass skins supported by urethane foam. Chordwise slots are cut into the trailing-edge cell so that the resulting structure consists of a series of spanwise pockets which function only as aerodynamic fairings. It does not contribute to the in-plane or torsional stiffness of the blade.

SPECIMEN DESIGN AND FABRICATION

To demonstrate the feasibility of the geodesic structural concept as a rotor blade damage-tolerant of 23mm HEI-T projectile impact, four full-scale blade specimens were fabricated.

The detailed specimen design is shown in Figure 24. This section is geometrically similar to the conceptual design in the region of Rotor Station 140, except for the elimination of twist and taper of the section to reduce the cost of manufacturing the specimens. The end fittings of the specimen were designed to be compatible with the U.S. Army Helicopter Main Blade Survivability Test Rig at the Ballistic Research Laboratories, Aberdeen Proving Ground, Maryland.¹²

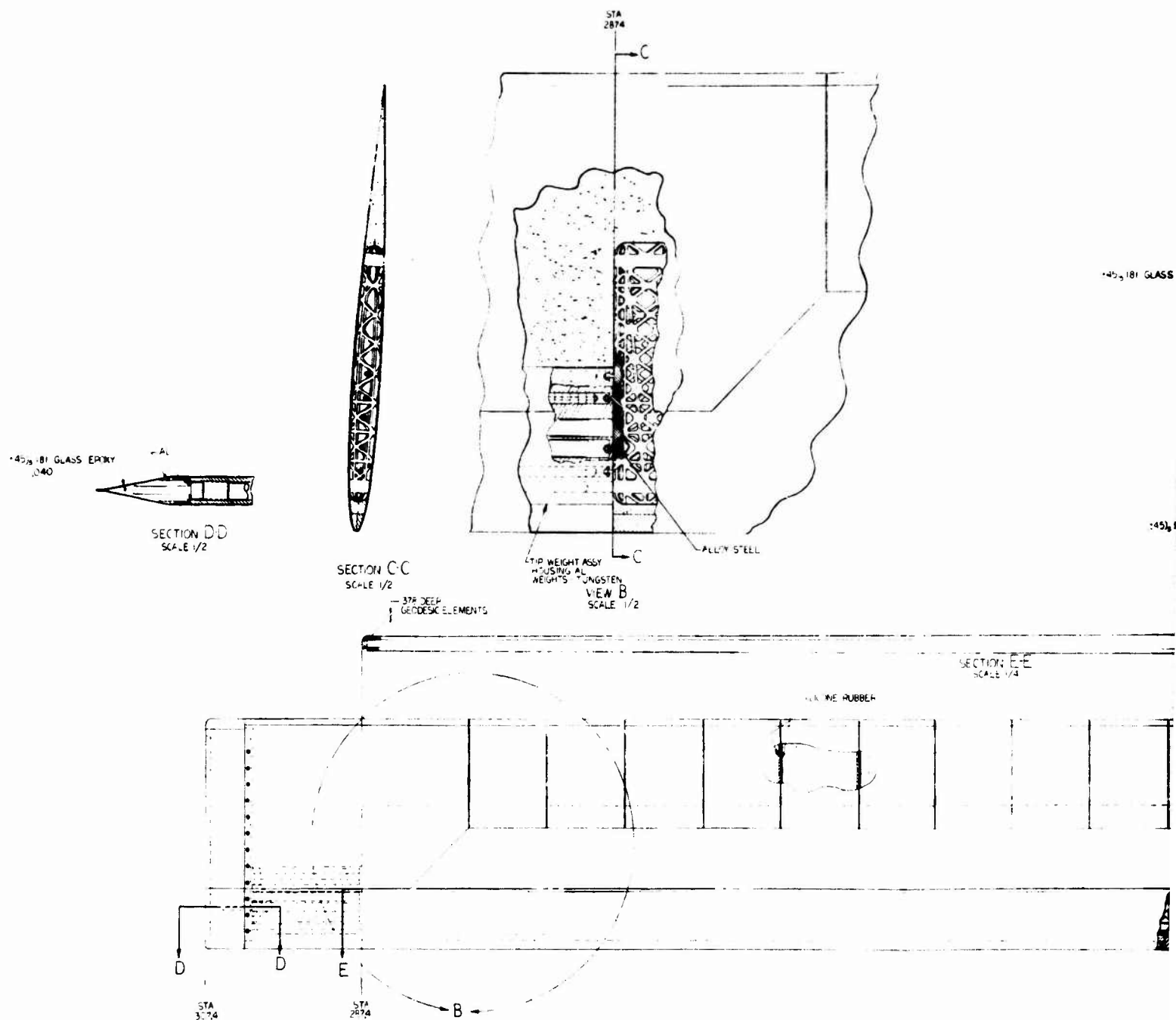
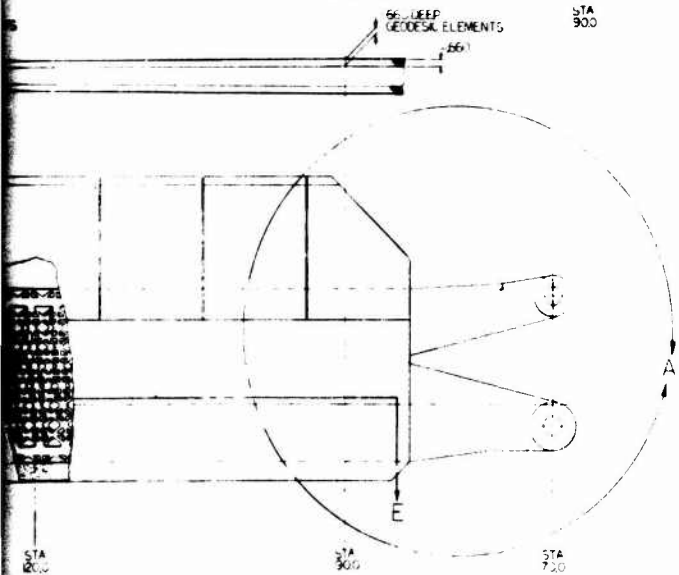
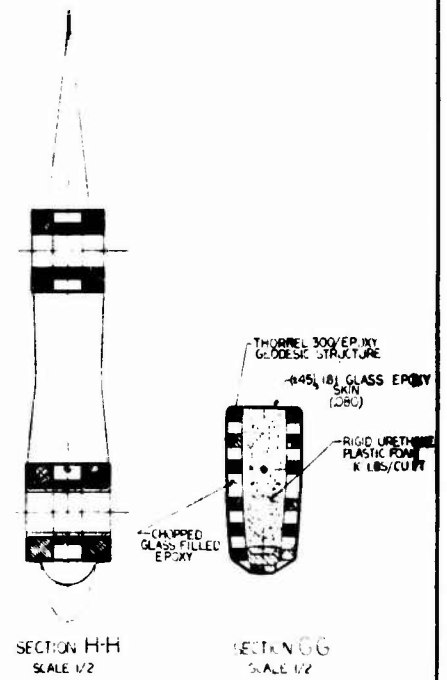
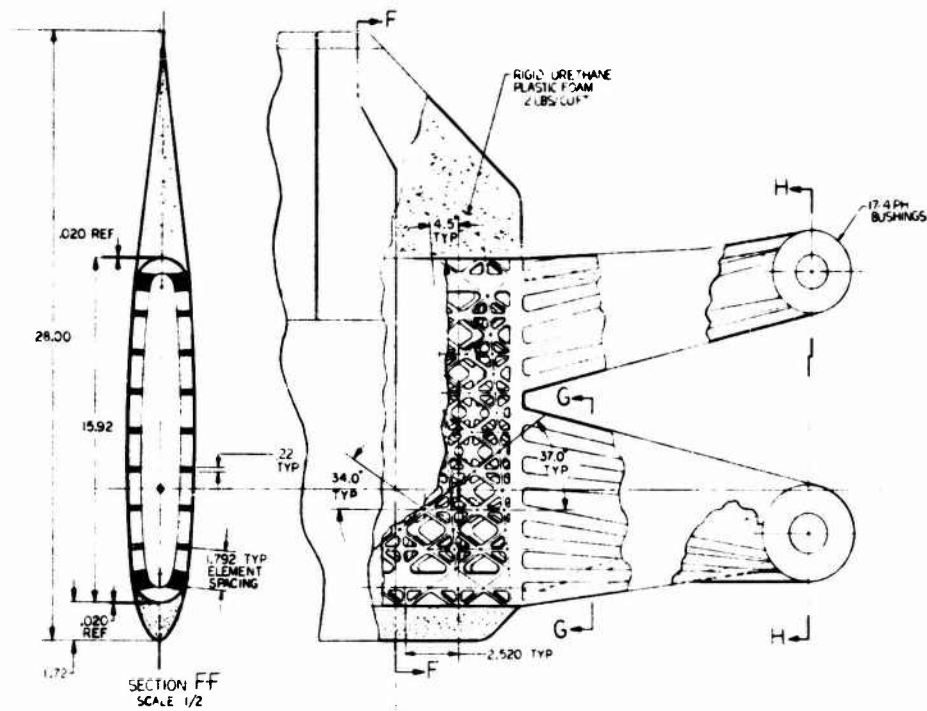


Figure 23. Conceptual Design of a Geodesic Rotor Blade.

BETWEEN STA 200 & STA 302.4



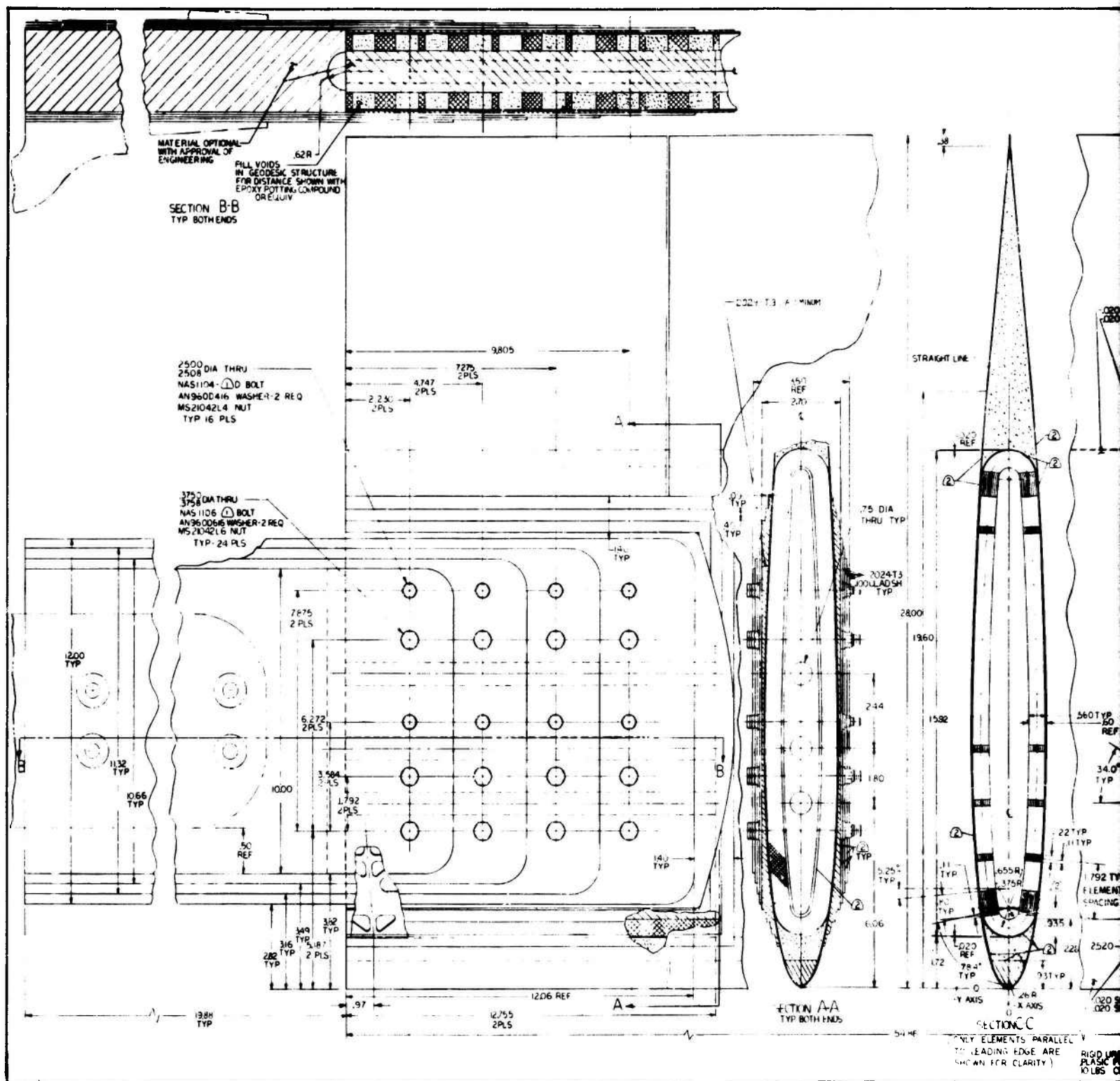
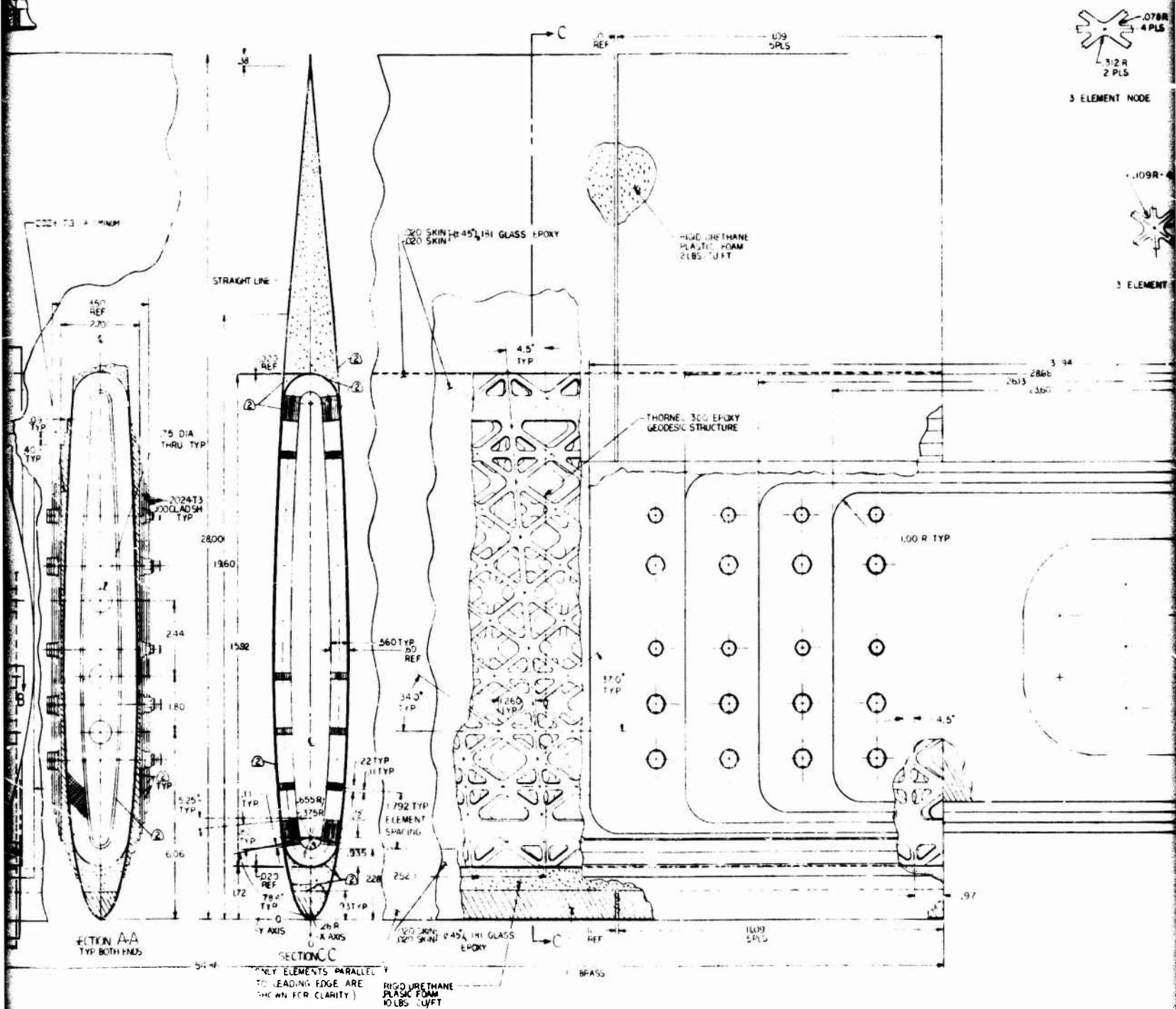
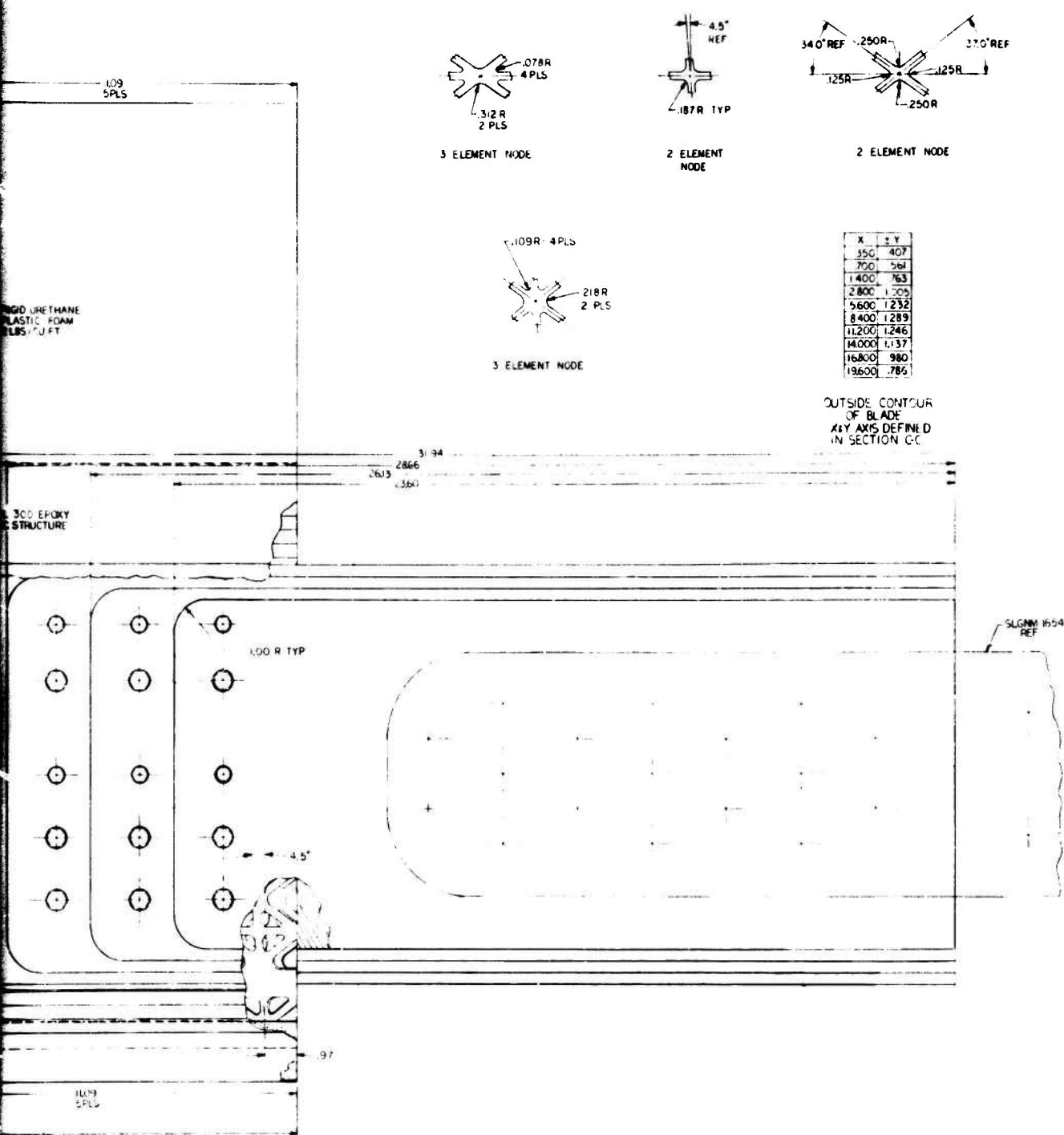


Figure 24. Geodesic Blade Segment Design.

Preceding page blank





② ADHESIVE
① GRIP LENGTH TO BE DETERMINED IN ASSY
NOTES

The blade specimens were fabricated in a manner similar to the subscale spar sections. A typical geodesic spar is shown in Figure 25, and the complete blade specimen is shown in Figure 26.

BALLISTIC TESTS

Three blade specimens as per Figure 24 were shipped to Ballistic Research Laboratories (BRL) and ballistically tested on Range 7 (see Figure 27) using the Helicopter Main Blade Ballistic Survivability Rig (MBBSR) described in Reference 12. Holes were drilled in the aluminum end plates of the specimens by BRL to match and to bolt on the MBBSR grips. Each specimen was pre-impact loaded to approximately 57,000 lb tension. This load represents a maximum level in-flight (V_{max}) centrifugal force (CF). No bending moments (flapwise or chordwise) were applied to the blade specimens. It was determined that such intentional bending would be transformed into an artificially high and unrealistic bending stress on the remaining blade structure after projectile ballistic impact. The reasons for the artificially high bending are the shortness of the specimens and the method by which the blade rig is used to apply bending loads.

The first specimen was impacted at an angle of 150° (the impact angle is the angle formed by the projectile trajectory and the blade chordline, with 0° impact being directly into the leading edge, 90° indicating impact into the bottom, and 180° being directly into the trailing edge). A 23mm HEI-T projectile with a MG 25 (delay) fuze was used for the test. In an effort to simulate a superquick high explosive (HE) projectile, which is considered to be the most devastating projectile threat to rotor blades and which would detonate upon contact with the blade specimen surface, a .040-in.-thick 202-T3 aluminum function plate was placed 9.5 in. in front of the impact point (this being an average delay distance for the MG 25 fuze for detonation of the projectile after contact with a surface). The striking velocity was about 2,900 feet per second, and the point of contact, which was set at 8 in. aft of the leading edge, actually occurred approximately 10 in. aft of the leading edge. The projectile did not detonate just inside the surface of the blade as expected, but the detonation occurred 0.5 to 1.0 in. in front of the surface of the blade, with the resulting entry and subsequent exit damage being much greater than that which is characteristic of a superquick HE projectile. Thus the test was not representative of contact detonation of an HE projectile. Photographs of the entry and exit damage are shown in Figures 28 and 29 respectively. The blast/fragmentation pattern can be seen in Figure 28 on the blade specimen skin surface as evidence of detonation occurring prematurely. Figure 30 is a cross-section drawing illustrating spar structural material remaining after the projectile detonation.

Following projectile impact, the load on the specimen dropped to approximately 9,000 lb. The blade was reloaded to failure, which occurred at 18,000 lb. The failure was not catastrophic, but rather exhibited a

Preceding page blank



Figure 25. Graphite/Epoxy Blade Spar.

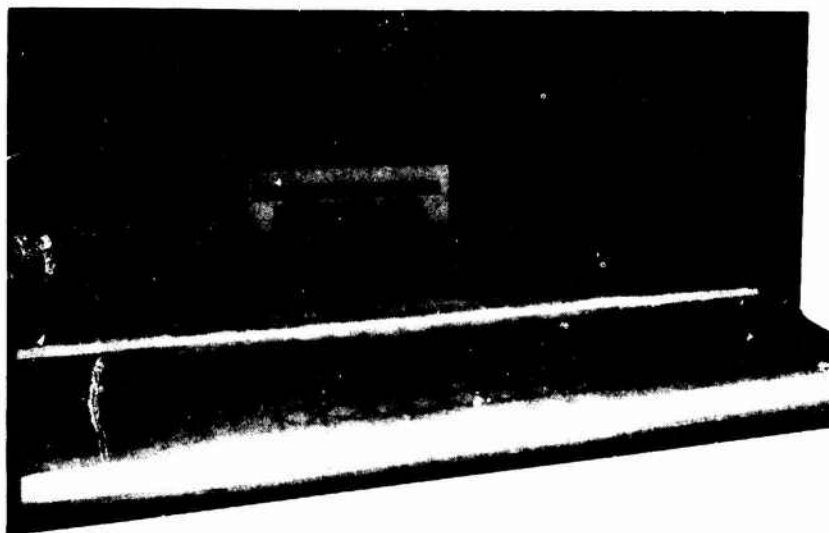


Figure 26. Geodesic Rotor Blade Segment.



Figure 27. Ballistic Range.



111874B1 E

LOCKHEED
CALIFORNIA COMPANY

SURVIVABLE

CONTRACT NO
DAAJ02-73-C-0101

PART NO
CL1702-1-6

BLADE NO 4

Reproduced from
best available copy.

Figure 28. Entry Damage - Specimen 1.



111874B1 +

Figure 29. Exit Damage - Specimen 1.

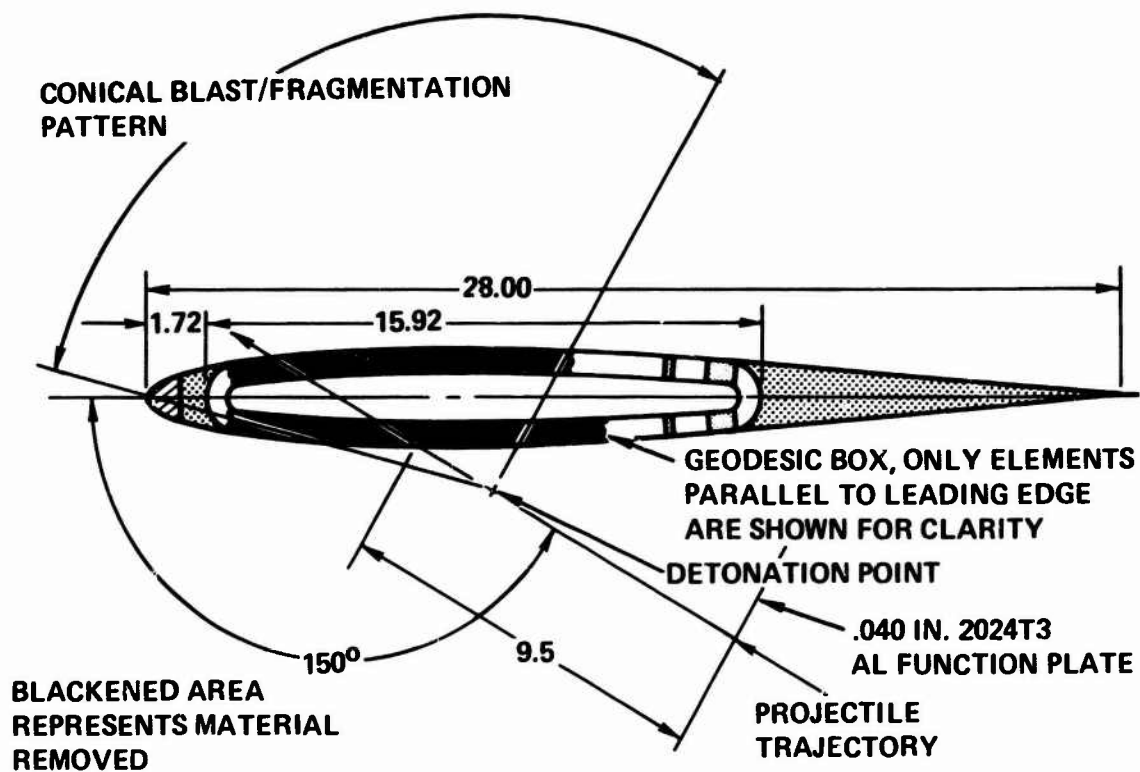


Figure 30. Ballistic Damage to Specimen 1.



Figure 31. Entry Damage - Specimen 2.

tearing, as individual elements within the geodesic box ruptured. Note that the removal of the unidirectional elements in the leading edge of the geodesic box caused a large shift in the neutral axis. Thus the applied tensile load induced a chordwise bending moment.

The second ballistic test specimen was impacted at an angle of 90° . The impact point was approximately 10 in. aft of the leading edge. To assure realistic detonation representative of a superquick fuze projectile, a 20mm M56E2 HEI projectile with a contact fuze was used for this test. Impact velocity was approximately 3,350 fps. After the impact, the load dropped to 50,000 lb and held there. The specimen was not reloaded to the original load or to failure in order to insure that a good damaged specimen that had survived ballistic tests be available for fatigue tests.

Photographs of the entry and exit damage are shown in Figures 31 and 32 respectively. Figure 33 is a photograph of a metal rotor blade which was impacted in a similar manner. Comparison of the damage indicates that the venting of the blast pressure in the geodesic open grid/frangible skin construction reduced the extent of the damage. A schematic of the remaining material within the blade is shown in Figure 34.

The third specimen was impacted at an angle of 30° with the impact point being 5.5 in. aft of the leading edge. A 23mm HEI-T projectile was used, with the MG 25 delay fuze again being functioned by a .040-in.-thick 2024T3 plate placed 8.0 in. in front of the specimen.

Examination of the damage shown in Figures 35, 36, and 37 indicates that this projectile also detonated too early, at about 0.5 to 1.0 in. in front of the surface of the blade. The load dropped to 6000 lb after projectile impact and was not reapplied in order to preserve the specimen for further inspection. Damage was extensive, almost identical to the first specimen tested, and again was not representative of a superquick-fuzed HE projectile. However, the test results from specimens 1 and 3 provide useful technological data despite the unsuccessful detonation points obtained on the blade specimens with the simulated 23mm HEI-T contact detonation fuze impacts. Inspection of the damaged blades reveals that the nose balance bar, which is a segmented nonstructural element, was intact. Had this component of the blade been integrated into the geodesic spar as a structural element, the blade could have survived the severe projectile impacts encountered. This implies that the brass bar should be replaced with unidirectional composite materials wound into the forward section of the geodesic spar, thus forming the balance bar as well as becoming part of the spar structural beam.

Ballistic test specimen 2 demonstrates the feasibility of using the geodesic open grid/frangible skin approach to minimize damage to the structure by HE projectile blast pressure. Unlike the damage caused to a metal blade by a similar shot, both the entrance and exit holes were relatively clean.



Figure 32. Exit Damage - Specimen 2.

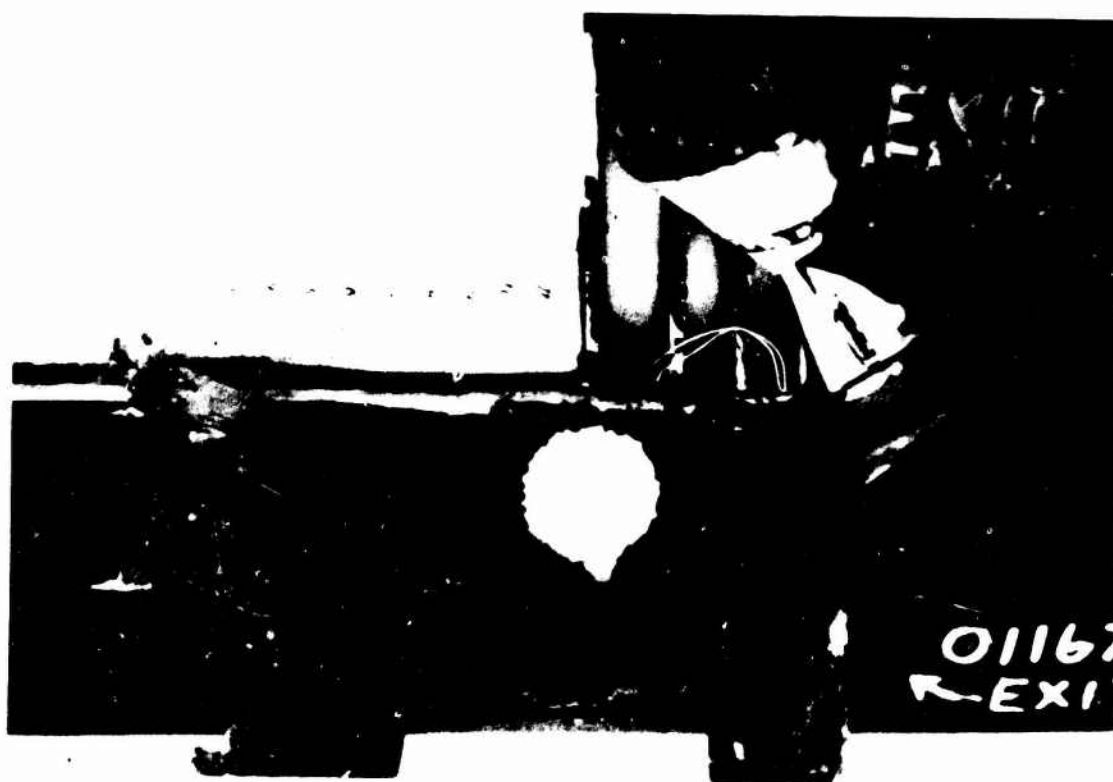


Figure 33. Damage to Metal Blade Caused By Ballistic Impact Similar to That Used on Specimen 2.

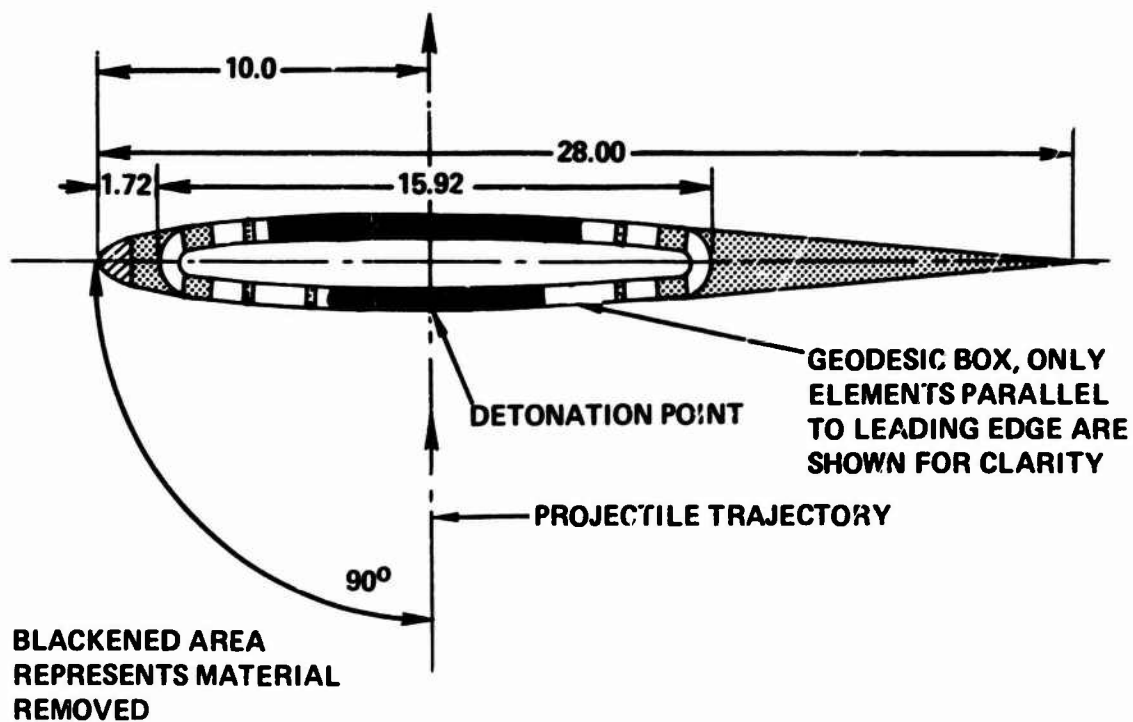


Figure 34. Ballistic Damage to Specimen 2.



Figure 35. Entry Damage - Specimen 3.

Reproduced from
best available copy.



112074 811815

Figure 36. Exit Damage - Specimen 3.

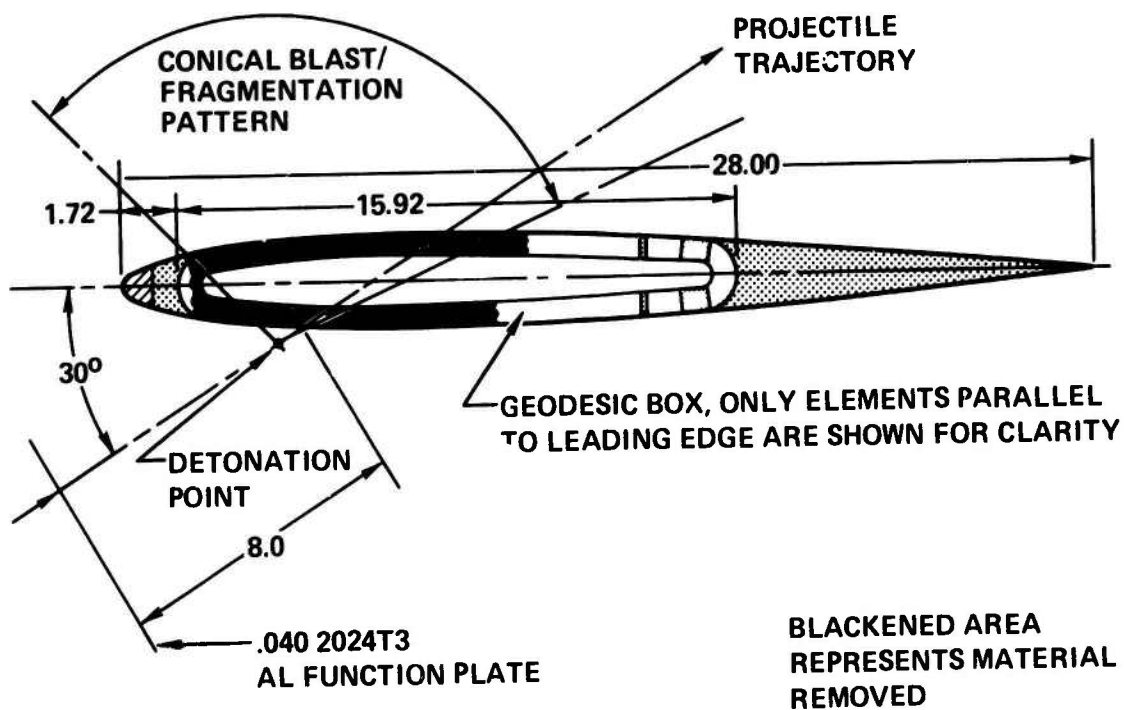


Figure 37. Ballistic Damage to Specimen 3.

STRUCTURAL TESTS

Two rotor blade specimens were subjected to structural testing: an undamaged blade and a 20mm HEI-T ballistic-damaged blade. Both specimens were subjected to fatigue loading followed by residual static strength tests. All structural tests on the blades were conducted at the Eustis Directorate, USAAMRDL. The fatigue testing was conducted on MTS 100 KIP Closed Loop Fatigue Test Equipment, and the residual strength testing was accomplished on Tinius Olson 300 KIP Testing Equipment.

Three strain gages were installed on each blade (see Table 6 for location). Axial strain data from these gages enabled calculation of the proportion of strain due to axial load, flapwise bending moment, and chordwise bending moment.

Blade specimens were subjected to tension-tension fatigue loading of 57,000 pounds + 28,000 pounds. This loading simulates flight loads at V_{max} , including centrifugal force, steady flapwise and chordwise bending, and cyclic flapwise and chordwise bending. Cyclic loading rates of 10 CPS and 7 CPS were used for the undamaged blade and damaged blade respectively. A photograph of the undamaged blade specimen installed in the fatigue test machine is shown in Figure 38.

The undamaged blade test specimen was tested for one million cycles. Both the applied loads and strains were recorded continuously throughout the test. Test results indicate that misalignment of the loading axis with respect to the blade neutral axis induced both flapwise and chordwise bending moments. Inspection of the specimen at about 13,000 cycles of the fatigue test revealed cracks in the leading-edge fiberglass skin at each joint of the segmented balance bars and some debonding of the grip plates. However, this type of damage was considered to be insignificant. Strain gage records indicate that no change in blade stiffness occurred as a result of the fatigue tests. A summary of the fatigue test data for the undamaged blade is presented in Table 6.

The 20mm HEI-T ballistic-damaged blade test specimen was fatigue tested in a manner identical to the undamaged blade. However, testing was terminated at the end of 342,000 cycles because excessive chordwise bending moments, induced by the offset of the load axis from the blade neutral axis, were causing large transverse loads in the load cell. This condition would have damaged the load cell; thus, the test was stopped.

The number of load cycles applied to the damaged blade far exceeded the 30-minute flight time requirement. Actually, the damaged blade specimen was calculated to have undergone over 23 hours of flight time. The test demonstrated that the blade test specimen was survivable. A summary of the fatigue test data for the damaged blade is presented

in Table 7. A photograph of the damaged blade after 327,000 cycles of fatigue loading is shown in Figure 39. Note that the blade skin has been cut away to enable inspection of the geodesic box spar.

After completion of the fatigue testing, the undamaged blade test specimen was placed in Tinius Olson 300 KIP Static Load Frame Test Equipment for residual strength testing. The complete test setup is shown in Figure 40. Two load cycles were required to fail the specimen. During the first test the specimen was loaded to a maximum tensile load of 235,750 pounds, at which time the aluminum end grip of the specimen connecting the crosshead of the test machine to the blade failed; see Figure 41. New steel grip plates for the blade ends were fabricated and installed and a second test was conducted. During this test the specimen reached a maximum load of 231,250 pounds before ultimate fracture occurred. Photographs of the fractured specimen are shown in Figures 42 and 43.

The load-strain curves of the two tensile tests are shown in Figure 44. Note that as the specimen approached the ultimate fracture load, the load-strain behavior became nonlinear, indicating progressive skin debonding and fiber breaks. Also note that some permanent damage was done to the specimen during the first test, since the results of the second test indicate a decrease in stiffness.

A static residual strength test was conducted on the damaged blade specimen. The specimen was loaded in tension until catastrophic failure occurred at 105,250 pounds. The fractured specimen is shown in Figures 45 and 46.

The load-strain curves of the tensile test on the damaged blade are shown in Figure 47. Unfortunately, strain gage #2 debonded at approximately 57,000 pounds. Thus, the failure strain of the longitudinal elements in the leading edge was not measured. The nonlinearity of the load strain curve as the specimen approached fracture indicates that progressive $\pm 35^\circ/90^\circ$ fiber failures were occurring.

The results of the static residual strength tests conducted on the undamaged and damaged blade specimens are summarized in Table 8. Also shown in Table 8 is the predicted static axial strength and stiffness of the blade specimens. Excellent correlation was obtained for predicted and measured axial stiffness in the undamaged and damaged blade specimens. However, the measured strength was lower than predicted for both blade specimens. This strength reduction is attributed to wrinkling of fiber bundles within the nodal regions and nonuniform yarn tension caused by hand-winding. It is interesting to note that the strength reduction factors observed for the blade specimens were lower than those of the subscale spar specimens described on page 37 of this report. This is probably due to the fact that only three elements intersected at a node in the blade specimens, whereas four elements intersected at a node

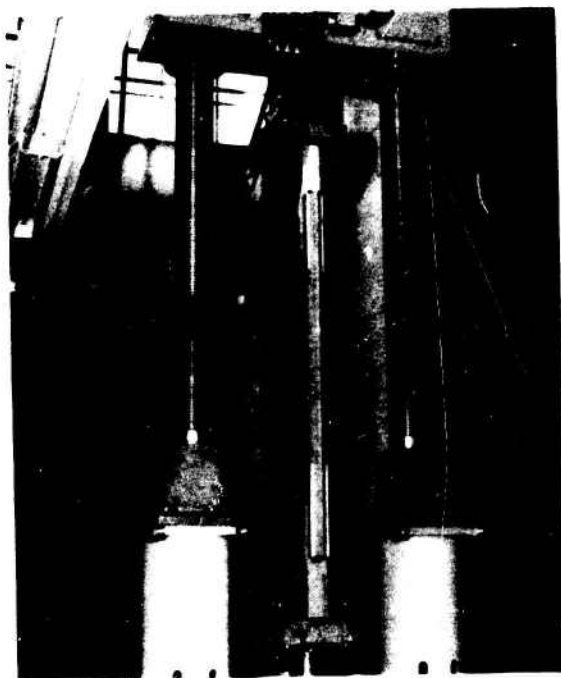


Figure 38. Undamaged Blade Installed in Fatigue Test Machine.

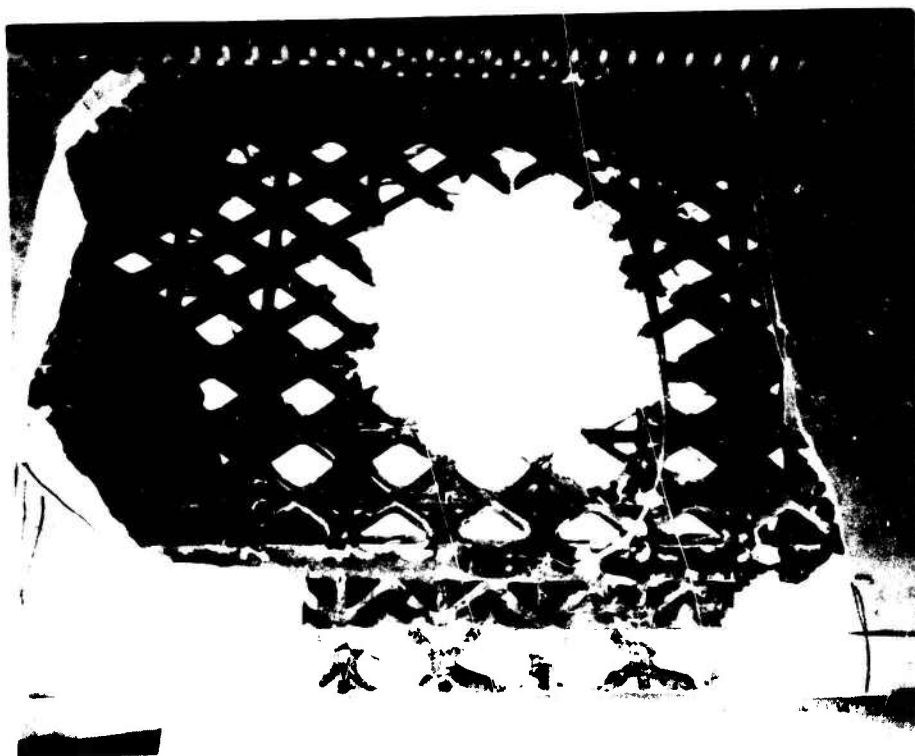
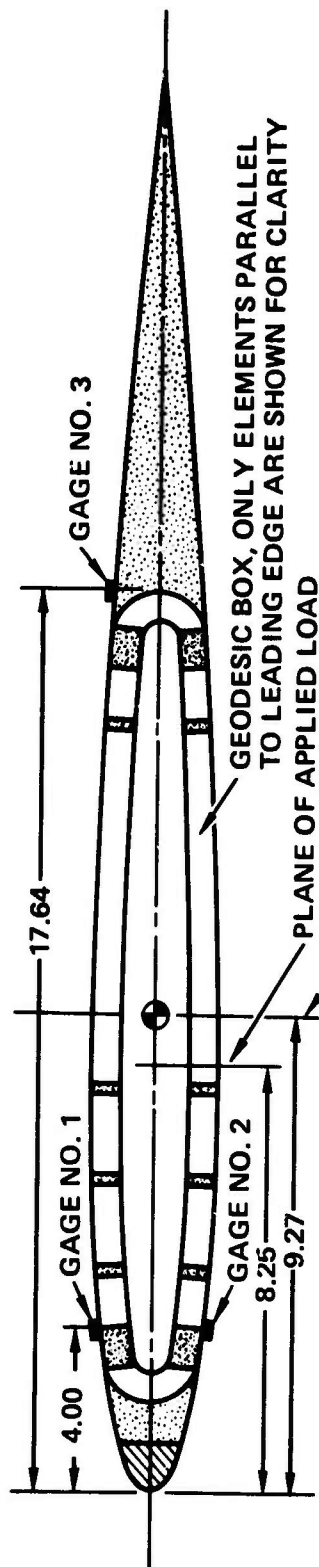


Figure 39. Exit Side of Damaged Blade After 327,000 Cycles of Load.

TABLE 6. SUMMARY OF FATIGUE TESTS ON UNDAMAGED BLADE



PREDICTED SECTION PROPERTIES*

$AE = 47.8 \times 10^6 \text{ LB}$
 $EI_f = 29.0 \times 10^6 \text{ LB-IN}^2$
 $EI_l = 18.0 \times 10^8 \text{ LB-IN}^2$

TEST DATA

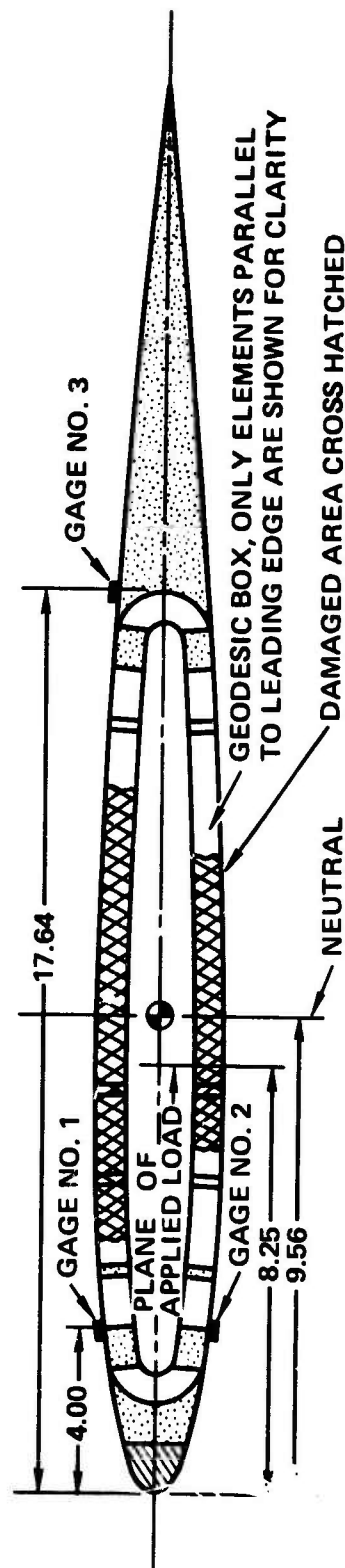
APPLIED LOAD = $57,000 \text{ LB} \pm 28,000 \text{ LB}$
 LOADING RATE = 10 CPS
 TOTAL CYCLES = 1,000,000

STRAINS (10^{-6} IN./IN.)	STRESS (KSI)
$\epsilon_1 = 1500 \pm 740$	$f_1 = 15.7 \pm 7.7$
$\epsilon_2 = 1270 \pm 620$	$f_2 = 13.3 \pm 6.5$
$\epsilon_3 = 820 \pm 400$	$f_3 = 8.6 \pm 4.2$

COMMENTS CRACKS IN FIBERGLASS SKIN, MINOR DEDONDING OF GRIPS OBSERVED DURING TESTS. NO CHANGE IN BLADE STIFFNESS AFTER 1,000,000 CYCLES

* FIBER VOLUME = 30% ELEMENT SIZE
 .20 IN. X .588 IN.

TABLE 7. SUMMARY OF FATIGUE TESTS ON DAMAGED BLADE



PREDICTED SECTION PROPERTIES*

AE = 36.67×10^6 LB
 $EI_f = 18.88 \times 10^6$ LB-IN.²
 $EI_j = 14.39 \times 10^8$ LB-IN.²

TEST DATA

APPLIED LOAD = $57,000 \text{ LB} \pm 28,000 \text{ LB}$
 LOADING RATE = 7 CPS
 TOTAL CYCLES = 342,000
 STRAINS (10^{-6} IN/IN) STRESS (KSI)
 $\epsilon_1 = 1350 \pm 660$ $f_1 = 14.1 \pm 6.9$
 $\epsilon_2 = 1700 \pm 830$ $f_2 = 17.8 \pm 8.7$
 $\epsilon_3 = 1050 \pm 520$ $f_3 = 11.0 \pm 5.4$

COMMENTS GAGE NO. 1 FAILED AT 5000 CYCLES, SLIGHT INCREASE IN STRAIN LEVEL IN GAGE NO. 2, NO CHANGE IN GAGE NO. 3.

* FIBER VOLUME = 30% ELEMENT SIZE
 .20 IN. X .588 IN.

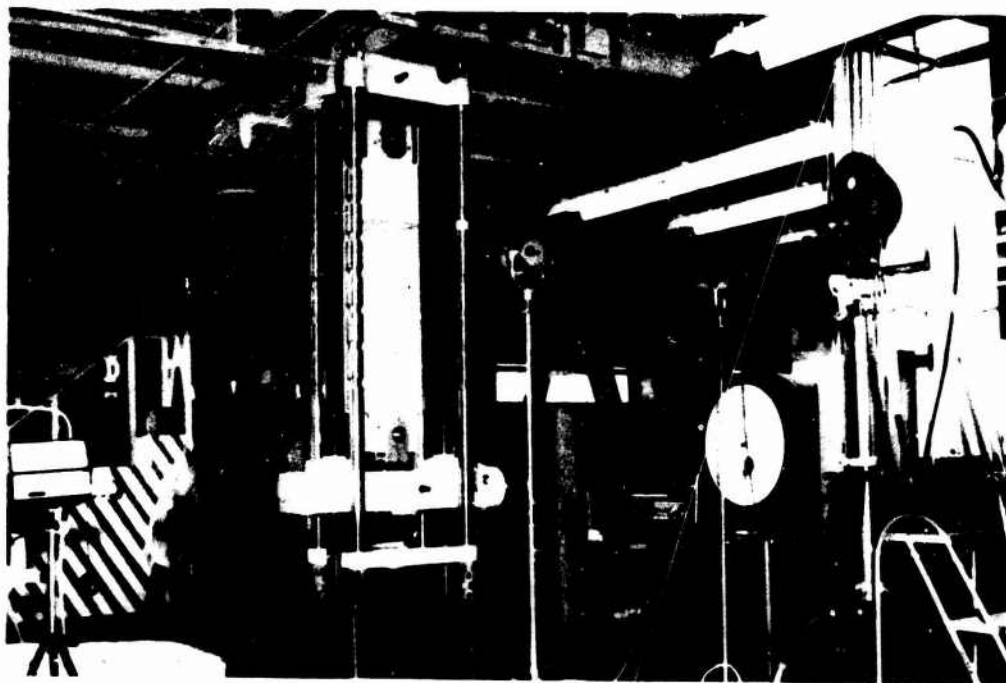


Figure 40. Residual Strength Test Apparatus.

Reproduced from
best available copy.



Figure 41. Undamaged Blade Specimen Aluminum End Grip Plate Failure.



Figure 42. Undamaged Blade Specimen After Residual Strength Test.

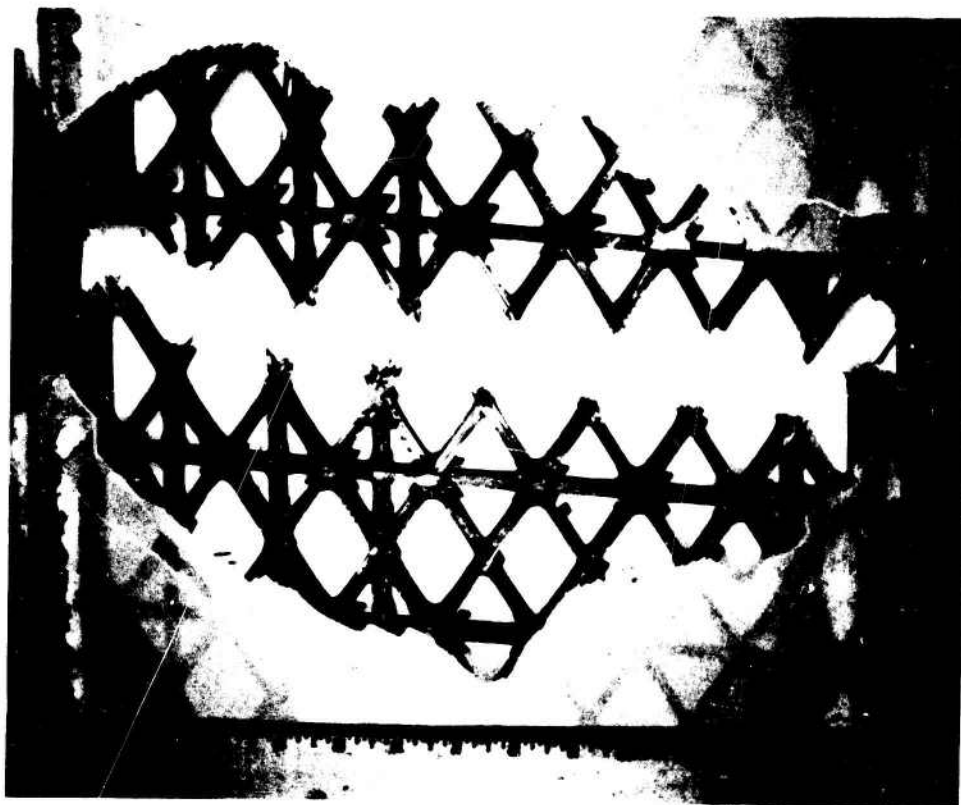


Figure 43. Fractured Surface in Geodesic Spar in Undamaged Blade Specimen.

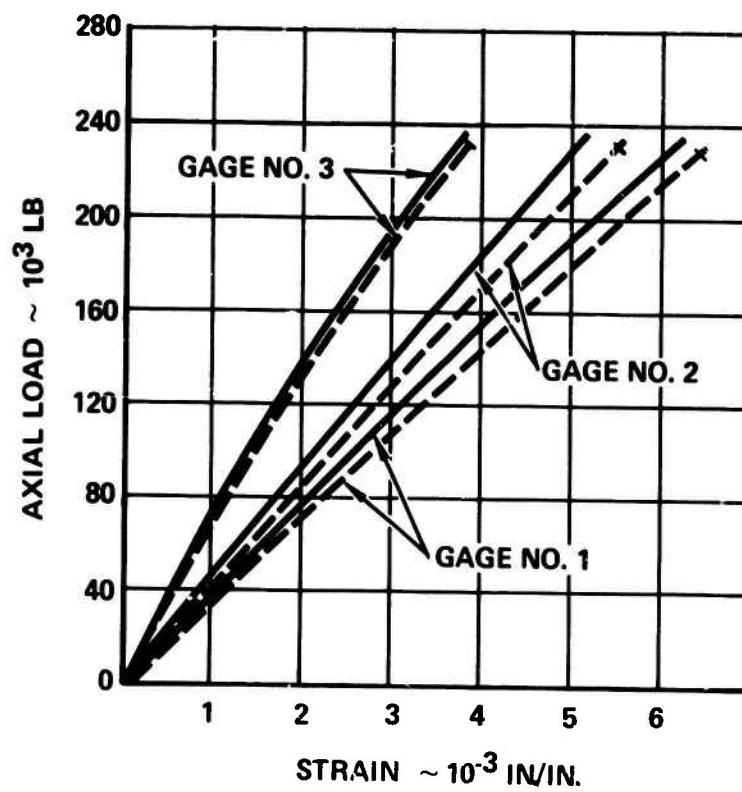


Figure 44. Undamaged Blade - Load-Strain Response.

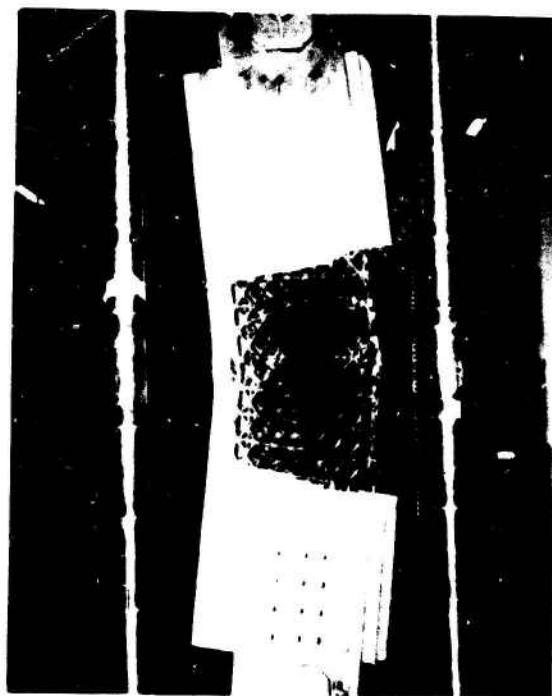


Figure 45. Damaged Blade Specimen After Residual Strength Test.



Figure 46. Fractured Surface in Geodesic Spar, Exit Side.

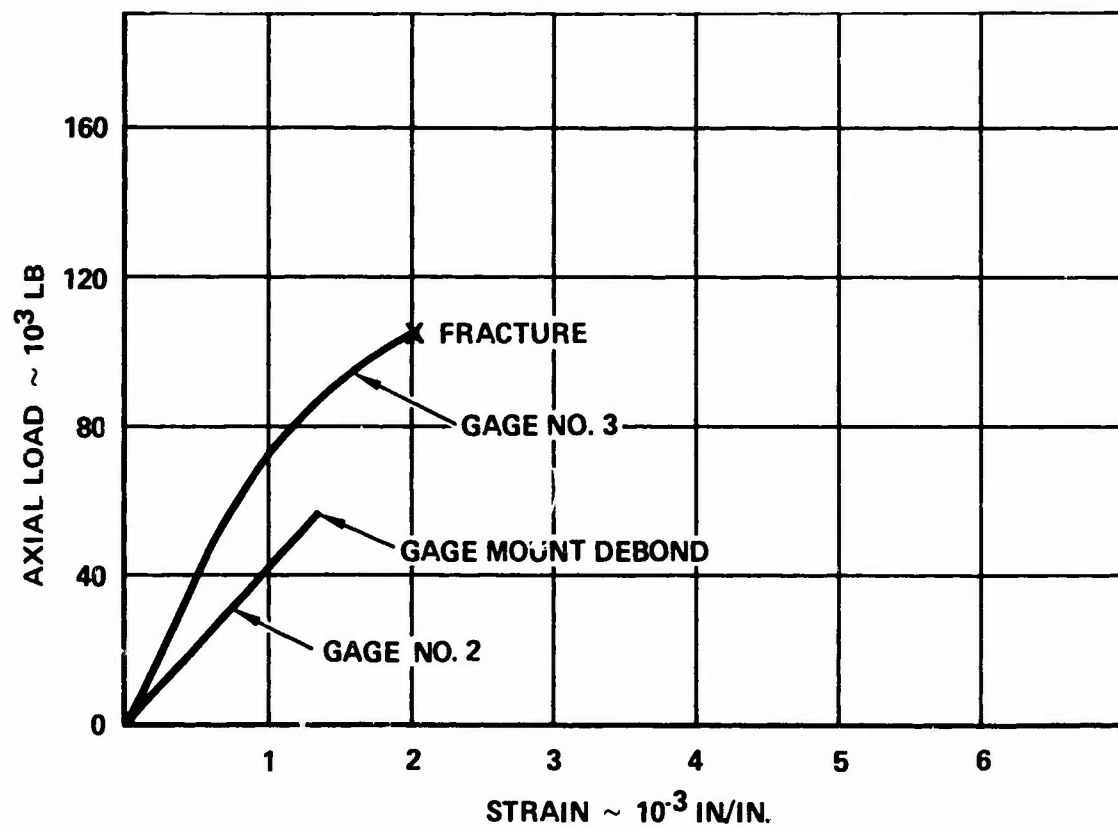


Figure 47. Damaged Blade - Load-Strain Response.

TABLE 8. SUMMARY OF RESIDUAL STRENGTH TESTS

SPECIMEN	①		① ②		MEASURED AXIAL FAILURE LOAD (10 ³ LB)	PREDICTED STRENGTH MEASURED STRENGTH
	PREDICTED AXIAL STIFFNESS, AE (10 ⁶ LB)	PREDICTED AXIAL FAILURE LOAD (10 ³ LB)	MEASURED AXIAL STIFFNESS, AE (10 ⁶ LB)	MEASURED AXIAL FAILURE LOAD (10 ³ LB)		
UNDAMAGED	47.85	351.12	49.26	235.75		1.45
DAMAGED	36.67	166.73 ③	39.04	105.25		1.58

NOTES:

- ① BASED ON AVERAGE FIBER VOLUME OF 30% AND ELEMENT SIZE OF .20 X .588 IN.
- ② INCLUDES EFFECT OF LOAD AXIS OFFSET FROM NEUTRAL AXIS
- ③ INCLUDES A STRENGTH REDUCTION FACTOR OF 55% TAKEN FROM FIGURE 15, RESIDUAL STRENGTH CURVE FOR DAMAGED ISOGRID PANELS

in the subscale spar specimens. However, it is evident that additional research and development should be conducted to eliminate the strength reductions caused by the nodal regions.

CONCLUSIONS

1. Fibrous composite materials can be utilized to construct efficient geodesic structures.
2. The graphite/epoxy structures fabricated and tested in this program demonstrated approximately 45% less strength than predicted by analysis. This is attributed to fiber bundle wrinkling within the nodal regions and nonuniform tension in the fibers because of the hand winding manufacturing process.
3. The geodesic open grid/frangible skin approach minimized damage to the structure by HE projectile blast pressure.
4. Static and fatigue tests on a ballistically damaged geodesic blade specimen have demonstrated the feasibility of this design concept to increase helicopter main rotor blade survivability.

RECOMMENDATIONS

1. Additional research and development is required to investigate the intersection of the elements to eliminate the strength reductions due to fiber wrinkling in the nodal regions.
2. A machine for automatically winding tubular fiber resin geodesic structures should be designed and developed.
3. The blade design should be modified to include structural leading and trailing edges.

REFERENCES

1. Anonymous, THE TRIUMPH OF THE "WELLINGTON" AND GEODESIC CONSTRUCTION, The Aeroplane, Nov 1940
2. NACA Report 1195, FORMULAS FOR THE ELASTIC CONSTANTS OF PLATES WITH INTEGRAL WAFFLE-LIKE STIFFENING, Langley Aeronautical Laboratory, Langley Field, Va., 1954
3. Legg, K. L. C., INTEGRAL CONSTRUCTION - A SURVEY AND AN EXPERIMENT, Jour. R. A. S., Vol. 58, No. 523, July 1954, pp. 485-503
4. Meyer, R. R., ISOGRID - A SIMPLE EFFICIENT, STIFFENING CONCEPT, AIAA/ASME/SAE 14th Structures Structural Dynamics and Materials Conference, March 1973
5. Figge, I. E., TETRA CORE, Shell Aviation News, 391-1971, pages 18-24
6. Figge, I. E., USAAMRDL TR 71-63, EVALUATION OF TWO BALLISTICALLY TOLERANT FORWARD BELL CRANK CONCEPTS FOR THE CH-47 HELICOPTER, Eustis Directorate, U.S. Army Air Mobility Research and Development Laboratory, Ft. Eustis, Va., Nov 1971, AD 893206L
7. Ashton, J. E., and Whitney, J. M., THEORY OF LAMINATED PLATES/PROGRESS IN MATERIALS SCIENCE SERIES, Vol. IV, Technomic Publishing Co., 1970
8. STRUCTURAL DESIGN GUIDE FOR ADVANCED COMPOSITE APPLICATIONS, VOL IV - MATERIALS, Air Force Materials Laboratory, Jan 1973
9. REVIEW OF DUPONT PRD 49 PROGRAM FOR AFML & AFFDC, DuPont Report, Sept 1977
10. PLASTICS FOR AEROSPACE VEHICLES, MIL-HDBK-17A, Jan 1971
11. Daniel, I. M., Rowlands, R. E., and Whiteside, J. B., STRESS CONCENTRATION AND STRENGTH REDUCTION IN COMPOSITE PLATES WITH CUTOUTS, Proceedings of the Conference on Fibrous Composites in Flight Vehicle Design, AFFDL-TR-72-130, Sept 1972
12. HELICOPTER MAIN BLADE BALLISTIC SURVIVABILITY RIG, Ballistic Research Laboratories, Aberdeen Proving Ground, Maryland, BRL CR 77, Sept 1972

APPENDIX A

COMPUTER PROGRAM FOR GEODESIC PLATES

This appendix contains the computer program developed to calculate the stiffness and strength of geodesic flat plates. The symbols used within the program and sample runs are also included.

PROGRAM INPUT

PHI	Angle between X and skewed elements (deg)
Px	Spacing of longitudinal elements (in.)
t	Thickness of geodesic plate (in.)
MODE	Input option: if MODE = 1, then input width of elements; if MODE \neq 1, then input volumetric percentage of elements and desired panel density.
bx, by, bphi	Width of elements (in.)
l, m, n	Volumetric percentage of elements in X, Y, and PHI directions respectively
RHOEFF	Effective density of plate (lb/in. ³)
Ex, Ey, Ephi	Axial moduli of elements in the X, Y, and PHI directions (psi)
RHOx RHOy RHOpHi	Density of elements in the X, Y and PHI directions (lb/in. ³)
NN	Applied panel line load, axial, transverse and shear (lb/in.)

PROGRAM OUTPUT

Py, phi	Spacing between elements in Y and PHI directions respectively (in.)
A	Extensional stiffness matrix (lb/in.)
D	Flexural stiffness matrix (lb-in.)
EX, EY	Plate tensile moduli along X axis and Y axis (lb/in. ²)
GXY	In-plane shear modulus of plate (lb/in. ²)
MUXY	Poisson's ratio of the plate
SPEC EX, SPEC EY	Plate specific stiffness along X and Y axes (lb)
SPEC GXY	Plate specific in-plane shear stiffness (lb)
STRSX, STRSY, STRSPH	Element stresses in the X, Y, and PHI directions for the applied loads

INTERNAL PROCEDURES

CGEN	Generates the extensional stiffness matrix of the elements referred to the axis of symmetry of the element C1 (lb/in.), and the flexural stiffness matrix of the elements referred to the axis of symmetry of the element C4 (lb/in.)
INVS	Inversion of a 3X3 matrix
ROTA	Rotation of element extensional and flexural stiffness matrices from the element axis of symmetry to the axis of symmetry of the plate.

PROGRAM LISTING

The computer program listing is reproduced in Figure A-1.

```

10. /* GEODES,CG */;
20. /* C F GRIFFIN D 68-21 X 8247 */;
30. /* STIFFNESS AND STRENGTH OF GEODESIC PLATES */;
40. DECLARE A(3,3) DEC(6),ASTAR(3,3) DEC(6),D(3,3) DEC(6)
    ,T(3,3) DEC(6);
50. DECLARE CC(6,6) DEC(6),CCC(6,6) DEC(6),C1(3,3) DEC(6)
    ,C4(3,3) DEC(6),AM(3,3) DEC(6),DM(3,3) DEC(6);
60. DECLARE EPS(3) DEC(6),EPST(3) DEC(6),NN(3) DEC(6);
70. GET LIST(PHI,Px,t,MODE);
80. tx,ty,tphi=t;
90. IF MODE=1 THEN GET LIST(bx,by,bphi); ELSE GET LIST(1,
    m,n,RHOEFF);
100. GET LIST(Ex,Ey,Ephi,RHOx,RHOy,RHOpHl);
110. GET LIST(NN);
120. STOP;
130. Py=Px*cosd(PHI)/sind(PHI);
140. Pphi=Px*cosd(PHI);
150. IF MODE=2 THEN GO TO M2;
160. A1=Py*bx*RHOx;
170. Am=Px*by*RHOy;
180. An=bphi*2*Px*RHOpHl/sind(PHI);
190. AA=A1+Am+An;
200. I=A1/AA*100;
210. m=Am/AA*100;
220. n=An/AA*100;
230. RHDEFF=AA/(Px*Py);
240. IF MODE=1 THEN GO TO M1;
250. AA=RHOEFF*Px*Py;
260. A1=I*AA/(100*RHOx);
270. Am=m*AA/(100*RHOy);
280. An=n*AA/(100*RHOpHl);
290. bx=A1/Py;
300. by=Am/Px;
310. bphi=An/(2*Px)*sind(PHI);
320. PUT LIST(LF(2));
330. PUT LIST(AST(30));
340. PUT IMAGE(PHI,Px,Py,Pphi,RHOEFF)(###);
350. IMAGE;
360. PHI = -- Px = ---- Py = ---- Pphi = ---- RHOEFF = ----
    PUT EDIT('ELEMENT','E','RHO','t','b','n')(SKIP(2),A(1
    0),X(5),(5) A(10));
370. PUT EDIT('x',Ex,RHOx,tx,bx,1)(A(10),(1) E(10,2),(4) F
    (10,4));
380. PUT EDIT('y',Ey,RHOy,ty,by,m)(A(10),(1) E(10,2),(4) F
    (10,4));
390. PUT EDIT('phi',Ephi,RHOpHl,tphi,bphi,n)(A(10),(1) E(1
    0,2),(4) F(10,4));
400. Ax=bx*tx/Px;
410. Ay=by*ty/Py;
420. CALL CGEN(Ex,Ey,Ax,Ay,tx,ty,bx,by,CC);
430. Aphi=bphi*tphi/Pphi;

```

Figure A-1. Program Listing (Sheet 1 of 4).

```

440. CALL CREN(Ephl,0,Aphl,0,hphl,0,hphl,0,ccc);
450. T(1,1),T(2,2)=COSD(PHI)*2;
460. T(1,2)=SIND(PHI)*2;
470. T(1,3)=2*SIND(PHI)*COSD(PHI);
480. T(2,3)=-T(1,3);
490. T(3,3)=T(1,1)-T(1,2);
500. T(2,1)=T(1,1);
510. T(3,2)=SIND(PHI)*COSD(PHI);
520. T(3,1)=-T(3,2);
530. DO I=1 TO 3;
540.   DO J=1 TO 3;
550.     C1(I,J)=CCC(I,J);
560.   END L1;
570. DO I=4 TO 6;
580.   DO J=4 TO 6;
590.     K=I-3;
600.     I1=J-3;
610.     C4(K,I1)=CCC(I,J);
620.   END L3;
630. CALL ROTA(C1,AM);
640. CALL ROTA(C4,DM);
650. DO I=1 TO 3;
660.   DO J=1 TO 3;
670.     A(I,J)=CC(I,J)*AM(I,J);
680.     K=J+3;
690.     I1=I+3;
700.     D(I,J)=CC(I1,K)*DM(I,J);
710.   END L4;
720. CALL INVS(A,ASTAR);
730. UT=1/EX;
740. PUT EDIT('A','D')(SKIP(2),X(23),A,X(42),A);
750. DO I=1,2,3;
760.   PUT IMAGE(A(I,1),A(I,2),A(I,3),D(I,1),D(I,2),D(I,3)
770.   )(#);
780. END;
790. # : IMAGE;
.....
.....
.....
800. EX=UT/ASTAR(1,1);
810. E=-UT/ASTAR(2,2);
820. MUXY=-ASTAR(1,2)/ASTAR(1,1);
830. GXY=UT/ASTAR(3,3);
840. PUT LIST(LF(2));
850. PUT IMAGE(EX,EY,MUXY,GXY,EX/RHOEFF,EY/RHOEFF,GXY/RHOE
FF)(#);
860. # : IMAGE;
870. EX = ..... EY = ..... MUXY = ..... GXY = ..... SPEC EX =
..... SPEC EY = ..... SPEC GXY = .....
880. PUT LIST(LF(2));
890. DO I=1,2,3;
EPS(I)=ASTAR(1,1)*NN(1)+ASTAR(1,2)*NN(2)+ASTAR(1,3)
*NN(3);

```

Figure A-1. Program Listing (Sheet 2 of 4).

```

900. END ;
910. STRSX=EPS(1)*Ex;
930. STRSY=EPS(2)*Ey;
950. DO I=1,2,3;
960. EPST(1)=T(1,1)*EPS(1)+T(1,2)*EPS(2)+T(1,3)*EPS(3);
970. END ;
980. STRSPH=EPST(1)*Ephi;
1000. IF bx=0 THEN STRSX=0;
1010. IF by=0 THEN STRSY=0;
1020. IF bphi=0 THEN STRSPH=0;
1030. PUT IMAGE(MN(1),MN(2),MN(3),STRSX,STRSY,STRSPH)(####)
;
1040. ##### IMAGE;
NX = ----- HY = ----- NXY = ----- STRSX = ----- STRSY =
----- STRSPH = -----
1050. PUT LIST(LF(2));
1060. STOP ;
1070. CGEN: PROCEDURE (E1,E2,A1,A2,t1,t2,h1,h2,C);
1080. C=0;
1090. C(1,1)=E1*A1;
1100. C(2,2)=E2*A2;
1110. C(4,4)=E1*t1+2*A1/12;
1120. C(5,5)=E2*t2+2*A2/12;
1140. RETURN ;
1150. END CGEN;
1160. INVS: PROCEDURE (X,Y);
1170. DETA=X(1,1)*X(2,2)*X(3,3)+X(1,2)*X(2,3)*X(3,1)+X(1,3)*X(2,1)*X(3,2)-
3)*X(2,1)*X(3,2);
DETA=DETA-X(1,3)*X(2,2)*X(3,1)-X(1,2)*X(2,1)*X(3,3)
-X(1,1)*X(2,3)*X(3,2);
Y(1,1)=(X(2,2)*X(3,3)-X(2,3)*X(3,2))/DETA;
Y(2,1)=-X(2,1)*X(3,3)-X(2,3)*X(3,1))/DETA;
Y(3,1)=-X(2,1)*X(3,2)-X(2,2)*X(3,1))/DETA;
Y(1,2)=-X(1,2)*X(3,3)-X(1,3)*X(3,2))/DETA;
Y(2,2)=(X(1,1)*X(3,3)-X(1,3)*X(3,1))/DETA;
Y(3,2)=-X(1,1)*X(3,2)-X(1,2)*X(3,1))/DETA;
Y(1,3)=-X(1,2)*X(2,3)-X(1,3)*X(2,2))/DETA;
Y(2,3)=-X(1,1)*X(2,3)-X(1,3)*X(2,1))/DETA;
Y(3,3)=(X(1,1)*X(2,2)-X(1,2)*X(2,1))/DETA;
END ;
1280. RETURN ;
1290. END INVS;
1300.
1310. ROTA: PROCEDURE (Q,QQ);
1320. QQ=0;
1330. DO Q=PHI,-PHI;
1340. mm=cosd(Q);
1350. nn=sind(Q);
1360. QQ(1,1)=QQ(1,1)+Q(1,1)*mm+4+2*(Q(1,2)+2*Q(3,3))*
nn+2*mm+2*Q(2,2)+Q(1,1)*nn+4;
1370. QQ(2,2)=QQ(2,2)+Q(1,1)*nn+4+2*(Q(1,2)+2*Q(3,3))*
nn+2*mm+2*Q(2,2)+Q(2,2)*mm+4;

```

Figure A-1. Program Listing (Sheet 3 of 4).

```

1380.      QQ(1,2)=QQ(1,2)+(Q(1,1)+Q(2,2)-4*Q(3,3))*NN**2*MM
**2*Q(1,2)*(MM**4+NN**4);
1390.      QQ(3,3)=QQ(3,3)+(Q(1,1)+Q(2,2)-2*Q(3,3))*NN**2*MM
**2*Q(3,3)*(MM**4+NN**4);
1400.      QQ(1,3)=QQ(1,3)+(Q(1,1)-Q(1,2)-2*Q(3,3))*NN*MM**3
+(Q(1,2)-Q(2,2)+2*Q(3,3))*NN**3*MM;
1410.      QQ(2,3)=QQ(2,3)+(Q(1,1)-Q(1,2)-2*Q(3,3))*NN**3*MM
+(Q(1,2)-Q(2,2)+2*Q(3,3))*NN*MM**3;
1420.      END ;
1430.      QQ(3,2)=QQ(2,3);
1440.      QQ(3,1)=QQ(1,3);
1450.      QQ(2,1)=QQ(1,2);
1460.      RETURN ;
1470.      END ROTA;
9999.      DECLARE CLEANP FILE;
1 -

```

Figure A-1. Program Listing (Sheet 4 of 4).

SAMPLE RUNS

For the example runs, the elements have been assumed to consist of intermediate-strength graphite/epoxy with a fiber volume of 50%. The predicted axial modulus, axial strength, and density of this material are the following:

$$E_{\text{BAR}} = 17.3 \times 10^6 \text{ psi}$$

$$F_{\text{BAR}} = 167.3 \times 10^3 \text{ psi}$$

$$\rho_{\text{BAR}} = .052 \text{ lb/in.}^3$$

Example 1

This plate has elements at $\pm 30^\circ$ and 90° in volumetric percentages of 66.67% and 33.33%, respectively. A segment of the structure is shown in Figure A-2. Note that in a typical cell, P_x by P_y , the total width of material oriented in the y direction is .20; thus $b_y = .20$ is input rather than the true width of the element in the y direction. The program input and output are shown in Figures A-3 and A-4.

Example 2

The addition of 0° elements to the plate of Example 1 results in a geodesic panel with 22.40% 0° , 25.87% 90° , and 51.73% $\pm 30^\circ$ elements. The input and output for this plate are shown in Figures A-5 and A-6.

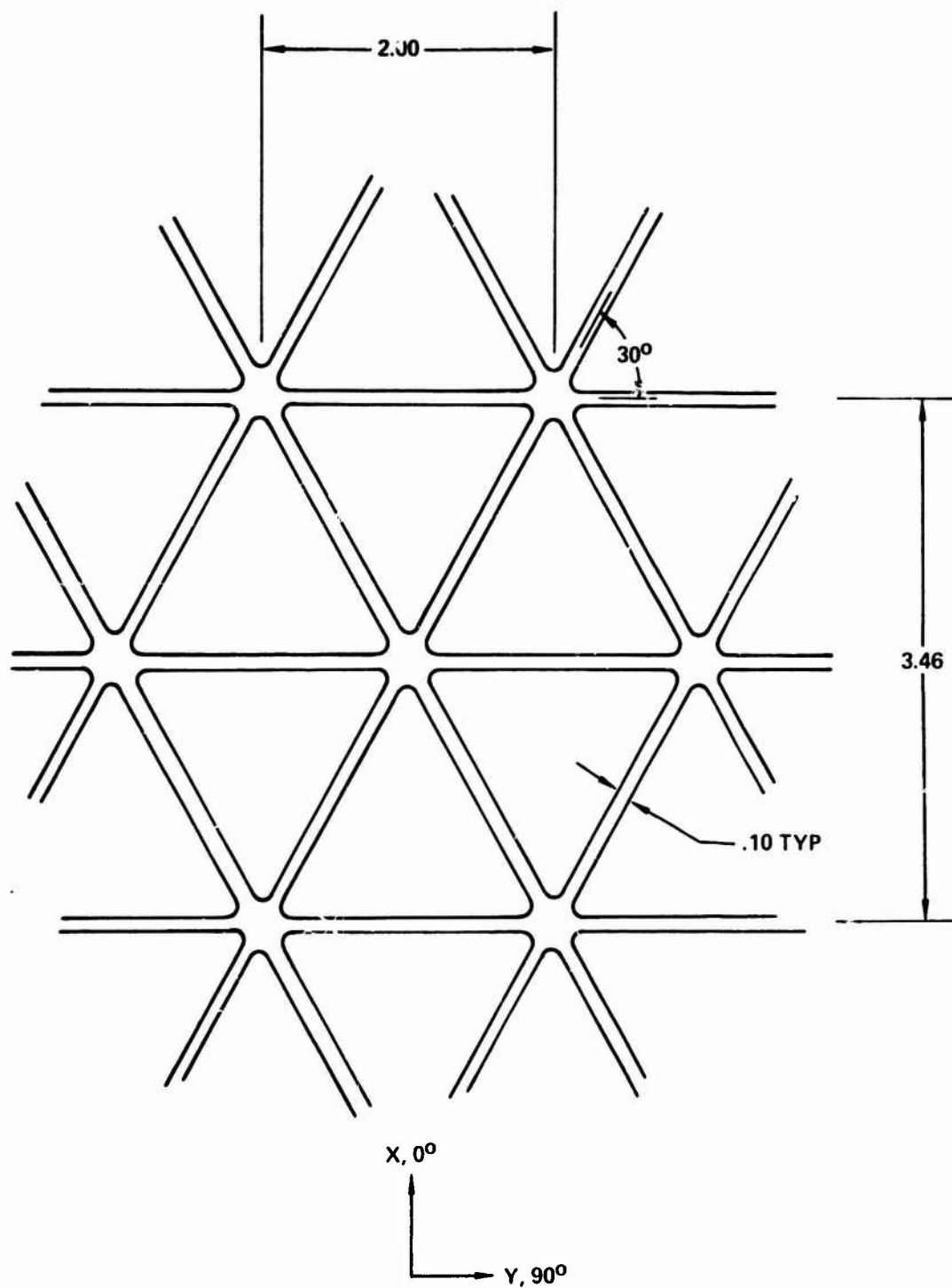


Figure A-2. Isogrid Structure From Example 1.

```

xeg
PHI
30
Px
2
+
5
McNE
1
bx
1
hy
2
bphl
1
Ex
17.3e6
Ev
17.3e6
Ephl
17.3e6
RHOX
.052
RHOY
.052
RHOPHI
.052
NN(1)
1000
NN(2)
0
NN(3)
0
** 120. XEQ "STOP".
-

```

Figure A-3. Computer Input, Example 1.

req* thru ...

 PHI = 30 Px = 2.0000 Py = 3.4641 Pphi = 1.7321 RHOEFF = 0.0116

ELEMENT	E	RHO	t	b	s
x	1.73E+07	0.0520	0.5000	0.1000	22.4009
y	1.73E+07	0.0520	0.5000	0.2000	25.8664
phi	1.73E+07	0.0520	0.5000	0.1000	51.7327

	A		D
.994334E06	.187278E06	-.47772E-01	.207153E05
.187278E06	.561634E06	-.29033E-02	.390162E04
-.47772E-01	-.29033E-02	.187278E06	.117049E05
			-.22325E-03
			.390162E04

EX = .1864E07 EY = .1053E07 MUXY = 0.3333 GXY = .3746E05 SPEC EX = .1606E09 SPEC EY = .9073E08 SPEC CXY = .3227E08

NX = 1000 NY = 0 NXY = 0 STRSX = 18564 STRSY = -6188 STRSPH = 12376

** 1060. XEQ "STOP".

Figure A-4. Computer Output, Example 1.

```

xeq
phi
30
p x
2
t
5
MODE
1
dx
0
by
2
bphi
1
ex
17.3e6
ey
17.3e6
ephi
17.3e6
rhox
.052
rhoxy
.052
rhophi
.052
nn(1)
1000
nn(2)
0
nn(3)
0
** 120. XEQ "STOP".

```

Figure A-5. Computer Input, Example 2.

```

xeq* thru ...

*****
PHI = 30 Px = 2.0000 Py = 3.4641 Pphi = 1.7321 RHOEFF = 0.0090

ELEMENT      E      RHO      t      b      s
x      1.73E+07      0.0520      0.5000      0.0000      0.0000
y      1.73E+07      0.0520      0.5000      0.2000      33.3333
phi     1.73E+07      0.0520      0.5000      0.1000      66.6667

          A          D
.561834E06      .187278E06      -.47772E-01      .117049E05      .390162E04      -.18146E-03
.187278E06      .561834E06      -.29033E-02      .390162E04      .117049E05      -.22325E-03
-.47772E-01      -.29033E-02      .187278E06      -.18146E-03      -.22325E-03      .390162E04

EX = .9988E06 EY = .9988E06 MUXY = 0.3333 GXY = .3746E06 SPEC EX = .1109E09 SPEC EY = .1109E09 SPEC CXY = .4159E08

NX = 1000 NY = 0 NXY = 0 STRSX = 0 STRSY = -11547 STRSPH = 23094

** 1060. XEQ "STOP".

```

Figure A-6. Computer Output, Example 2.

LIST OF SYMBOLS

A_{ij}	- Extensional stiffness matrix of the plate (lb/in.)
B_{ij}	- Coupling matrix (lb)
b_x, b_y, b_{PHI}	- Element widths (in.)
C_{ij}	- Extensional stiffness matrix referred to the axis of symmetry of element (lb/in.)
C'_{ij}	- Extensional stiffness matrix referred to the principal axis of plate (lb/in.)
D_{ij}	- Flexural stiffness matrix of the plate (lb-in.)
E_{BAR}	- Element tensile modulus along longitudinal axis (lb/in. ²)
E_f	- Fiber modulus (lb/in. ²)
E_m	- Matrix modulus (lb/in. ²)
E_x, E_y	- Plate tensile modulus along X axis and Y axis (lb/in. ²)
F_{BAR}	- Element tensile strength along longitudinal axis (lb/in. ²)
F_x	- Plate tensile strength along X axis (lb/in. ²)
G_{xy}	- In-plane shear modulus of plate (lb/in. ²)
K_{ij}	- Flexural stiffness matrix X referred to the axis of symmetry or element (lb-in.)
K'_{ij}	- Flexural stiffness matrix referred to the principal axis of the plate (lb-in.)
$M = \begin{bmatrix} M_x \\ M_y \\ M_{xy} \end{bmatrix}$	- Bending and twisting matrix (in.-lb/in.)
$N = \begin{bmatrix} N_x \\ N_y \\ N_{xy} \end{bmatrix}$	- In-plane force matrix (lb-in.)

LIST OF SYMBOLS (Continued)

P_x, P_y	- Element spacing (in.)
t	- Element depth (in.)
T_{ij}	- Transformation matrix
V_f	- Fiber volume
$\epsilon = \begin{bmatrix} \epsilon_x \\ \epsilon_y \\ \epsilon_{xy} \end{bmatrix}$	- In-plane strain matrix (in./in.)
μ_{xy}	- Major Poisson ratio of the plate
ρ_{EFF}	- Effective density of plate (lb/in. ³)
ρ_{BAR}	- Density of element (lb/in. ³)
ϕ	- Element orientation (°)
$\chi = \begin{bmatrix} \chi_x \\ \chi_y \\ \chi_{xy} \end{bmatrix}$	- Curvature and twist matrix (1/in.)